© 2016. Published by The Company of Biologists Ltd | Development (2016) 143, 1192-1204 doi:10.1242/dev.129825

RESEARCH ARTICLE

Grainyhead-like 2 downstream targets act to suppress epithelial-to-mesenchymal transition during neural tube closure

Heather J. Ray and Lee A. Niswander*

ABSTRACT

The transcription factor grainyhead-like 2 (GRHL2) is expressed in non-neural ectoderm (NNE) and *Grhl2* loss results in fully penetrant cranial neural tube defects (NTDs) in mice. GRHL2 activates expression of several epithelial genes; however, additional molecular targets and functional processes regulated by GRHL2 in the NNE remain to be determined, as well as the underlying cause of the NTDs in *Grhl2* mutants. Here, we find that *Grhl2* loss results in abnormal mesenchymal phenotypes in the NNE, including aberrant vimentin expression and increased cellular dynamics that affects the NNE and neural crest cells. The resulting loss of NNE integrity contributes to an inability of the cranial neural folds to move toward the midline and results in NTD. Further, we identified *Esrp1*, *Sostdc1*, *Fermt1*, *Tmprss2* and *Lamc2* as novel NNE-expressed genes that are downregulated in *Grhl2* mutants. Our *in vitro* assays show that they act as suppressors of the epithelial-to-mesenchymal transition (EMT). Thus, GRHL2 promotes the epithelial nature of the NNE during the dynamic events of neural tube formation by both activating key epithelial genes and actively suppressing EMT through novel downstream EMT suppressors.

KEY WORDS: Neural tube closure, Non-neural ectoderm, Epithelial-to-mesenchymal transition, Neural crest cells, *Grhl2*, *Trim29*, Mouse

INTRODUCTION

Neural tube closure (NTC) is a crucial embryological event that generates the primordia of the central nervous system. Complex molecular, cellular and tissue events must be coordinated to complete NTC correctly, and this complexity is reflected in the high frequency of neural tube defects (NTDs), a class of birth defects resulting from failure of NTC (Wilde et al., 2014; Copp et al., 1990, 2003). At the tissue level, NTC starts when the flat sheet of neuroectoderm (NE) bends at the median hinge point to elevate the neural folds. The neural folds then bend again at the dorsal-lateral hingepoints and come into contact at the midline. The NE separates from the non-neural ectoderm (NNE) and these tissues seal to form a closed neural tube (NT) with an overlying epithelial layer. The neural crest cells (NCCs) located at the NE/NNE border delaminate as the neural folds begin to close and then the NCCs migrate to distal sites to generate a number of different structures. The NE, NNE and NCCs all arise from the same continuous epithelial layer but they adopt different cellular morphologies. Whereas NE and NNE cells remain epithelial (pseudostratified columnar and squamous, respectively), NCCs undergo an epithelial-to-mesenchymal transition (EMT) and delaminate from the underlying basement membrane. These cellular changes are governed by the underlying molecular changes that promote these different cell fates.

The correct molecular and cellular regulation of these three distinct tissues is crucial, and studies from model systems have investigated how each tissue contributes to proper NTC. The NNE plays several roles in NT development, including proper patterning of the dorsal NT (Dickinson et al., 1995) and induction of the NCCs (Selleck and Bronner-Fraser, 1995). The NNE is positioned first lateral to, then overlying, the NE, and it also plays a key role in bringing the neural folds together. Studies in amphibians and chicks showed that removal of NNE from the developing neural folds inhibits their elevation and convergence toward the midline, while inclusion of only a small strip of NNE lateral to the NE allows for full NTC (Hackett et al., 1997; Jacobson and Moury, 1995; Moury and Schoenwolf, 1995). This ability of a small piece of NNE to promote full NTC was also seen in mouse NTC in the spinal region (Ybot-Gonzalez et al., 2002). While it has been proposed that this is due to a pushing force of the NNE against the NE, including NNE medial expansion and oriented cell division (Hackett et al., 1997; Morita et al., 2012; Sausedo et al., 1997), or to its signaling properties (Ybot-Gonzalez et al., 2002), the underlying molecular mechanisms within the NNE that promote NTC remain unclear.

An important molecular player within the NNE is the transcription factor (TF) grainyhead-like 2 (GRHL2). In mouse, *Grhl2* is expressed in many embryonic and adult epithelial tissues, and loss of *Grhl2* function in the NNE results in fully penetrant NTDs (Gustavsson et al., 2008; Pyrgaki et al., 2011; Rifat et al., 2010; Werth et al., 2010). GRHL2 directly regulates genes that are essential for epithelial fate, such as those encoding E-cadherin (cadherin 1), claudin 3 and claudin 4 (Mostov et al., 2012; Werth et al., 2010), and other epithelial genes are downregulated in *Grhl2* loss-of-function embryos (Pyrgaki et al., 2011). Despite the knowledge of these and other (Chen et al., 2012; Gao et al., 2013; Walentin et al., 2015) GRHL2-regulated downstream processes, it remains to be determined how *Grhl2* loss in the NNE leads to failure of NTC. Thus, continuing studies of GRHL2 function could shed light on the molecular processes that underlie NNE-driven NTC.

Clues as to how GRHL2 functions during development can be found in recent work that implicate it as a tumor suppressor in some epithelial cancers (Cieply et al., 2012; Xiang et al., 2013). The Claudin-low subtype of breast cancer expresses low levels of GRHL2, E-cadherin and claudin 4, is highly metastatic, and *GRHL2* expression positively correlates with distant metastasis-free survival (Cieply et al., 2012, 2013; Mlacki et al., 2015). GRHL2 acts as a suppressor of EMT in breast cancer cell lines and can directly repress the EMT-promoting TF *ZEB1* (Cieply et al., 2012, 2013). Additionally, GRHL2 knockdown in IMCD-3 kidney epithelial cells caused increased expression of the EMT-associated genes vimentin and *Twist2*, although not through direct transcriptional repression by

Department of Pediatrics, Cell Biology Stem Cells and Development Graduate Program, University of Colorado Anschutz Medical Campus and Children's Hospital Colorado, Aurora, CO 80045, USA.

*Author for correspondence (Lee.Niswander@ucdenver.edu)

Received 25 August 2015; Accepted 16 February 2016

Development (2016) 143, 1192-1204 doi:10.1242/dev.129825

GRHL2 (Aue et al., 2015). Although GRHL2 can act as a direct transcriptional repressor (Cieply et al., 2012), combined ChIP-seq and gene expression profiling revealed that it acts predominately through direct target activation (Gao et al., 2013; Walentin et al., 2015). This suggests that GRHL2 might activate EMT suppressors, which themselves normally modulate mesenchymal gene expression, and these alterations in EMT regulation within the NNE could have consequences for epithelial integrity that impact NTC.

Here we studied mouse NTC in *Grhl2* mutants and found that NNE cells lose epithelial integrity and gain mesenchymal characteristics. This disrupts the structure of the NNE and increases dynamic behavior, which contributes to an inability of the neural folds to meet at the midline, thus appearing to be the primary cause of NTDs. We identified a set of novel GRHL2-regulated genes expressed within the NNE that act as EMT suppressors and could promote NNE epithelialization, thus contributing to NTC. Our work highlights that embryonic epithelialization may be achieved by coordinating active promotion of epithelial fate with suppression of mesenchymal fate by the activation of a network of EMT suppressors.

RESULTS

Epithelial integrity of the NNE is lost in *Grhl2*$^{1Nisw/1Nisw}$ mouse embryos

GRHL2 regulates the development of many epithelial tissues, with loss of function leading to multiple defects in mice, including cranial NTD (Pyrgaki et al., 2011; Rifat et al., 2010; Werth et al., 2010). The *Grhl2*^{1Nisw} line was generated by ENU mutagenesis, and homozygous mutants exhibit fully penetrant exencephaly from the hindbrain through the forebrain (Pyrgaki et al., 2011). *Grhl2* is expressed in the NNE during NTC and is required for E-cadherin expression in the NNE (Pyrgaki et al., 2011). However, how loss of *Grhl2* affects NNE function and how this leads to NTD remain unknown.

Histological examination of the cranial neural folds of 13-somite wild-type embryos showed that NNE cells are tightly connected within the squamous epithelial layer in both the forebrain and hindbrain regions, where the folds have yet to meet but are converging toward the midline (Fig. 1A,C, arrows). However, in *Grhl2*$^{1Nisw/1Nisw}$ embryos some NNE cells are not connected with their neighbors and have a more mesenchymal appearance

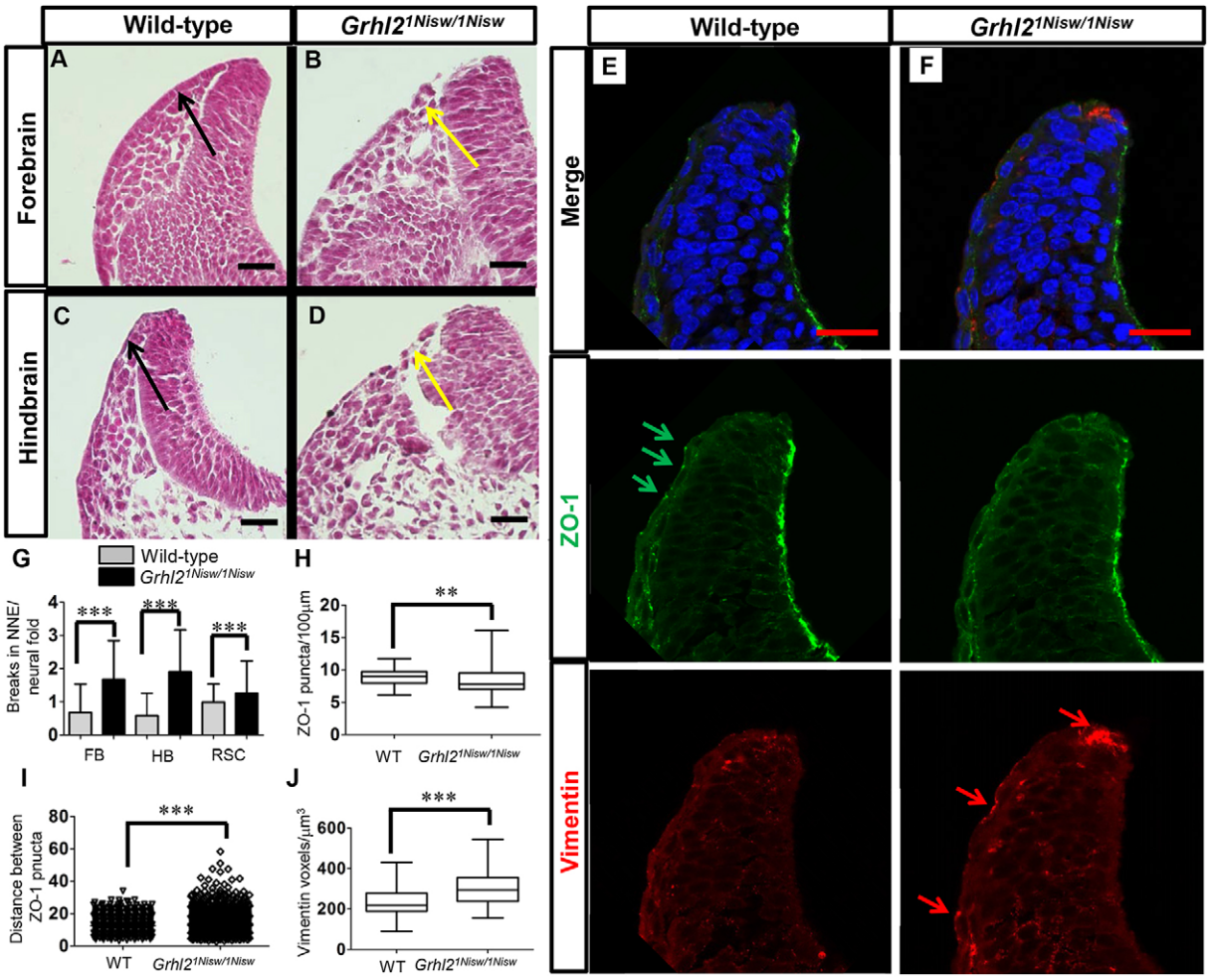

Fig. 1. *Grhl2* mutant NNE exhibits loss of epithelial integrity and increased mesenchymal properties. (A-D) H&E staining of transverse sections of cranial neural folds of 13-somite mouse embryos shows tightly associated wild-type NNE (A,C, arrows) versus the loosely associated epithelium and altered cellular phenotype of *Grhl2* mutant NNE (B,D, arrows). (E,F) Immunostaining shows regular, punctate ZO-1 (green arrows) and low-level vimentin expression in wild-type NNE (E) versus an irregular ZO-1 expression pattern and aberrant vimentin (red arrows) in *Grhl2* mutant NNE (F). (G-J) Quantitation of A-F. (G) NNE breaks in *Grhl2* mutants (seven embryos, 50 sections each) are increased compared with wild type (five embryos, 50 sections each). (H,I) The number of ZO-1 puncta per 100 µm shows greater spread and overall smaller mean (H) and the distance between puncta is greater in *Grhl2* mutant embryos than in wild type (I). (J) Vimentin expression is increased in *Grhl2* mutant NNE compared with wild type. Experiments were performed on four embryos per genotype, ten sections each. Mean±s.d. ***P*<0.001, ****P*<0.0001, Student's *t*-test. FB, forebrain; HB, hindbrain; RSC, rostral spinal cord; NNE, non-neural ectoderm; WT, wild type. Scale bars: 20 µm.

Development (2016) 143, 1192-1204 doi:10.1242/dev.129825

(Fig. 1B,D, arrows). The number of breaks between NNE cells within a 20-cell distance of the neural fold tips is significantly greater in *Grhl2*$^{1Nisw/1Nisw}$ compared with wild type in 13- to 18-somite embryos in all regions examined (Fig. 1G). Moreover, the folds in mutant embryos do not bend dorsolaterally to the extent seen in wild type, similar to neurulating chick embryos upon NNE removal (Hackett et al., 1997). Wild-type NNE exhibits a regular pattern of punctate zona occludens (ZO-1; TJP1 – Mouse Genome Informatics) expression, indicating the tight junctions and a close association between NNE cells, and they do not express the mesenchymal filamentous protein vimentin above background levels (Fig. 1E). *Grhl2* mutant NNE expresses ZO-1 but the regular punctate pattern is disrupted (Fig. 1F). In *Grhl2* mutant embryos, the number of puncta per 100 µm of NNE has both a broader range and decreased mean (Fig. 1H) and the distance between puncta is significantly increased (Fig. 1I) compared with wild type, indicating an irregular distribution of tight junctions. *Grhl2* mutant NNE also expresses significantly more vimentin than in wild-type embryos, with the highest levels at the neural fold tips (Fig. 1F,J). Thus, loss of *Grhl2* causes NNE cells to change their molecular profile and lose epithelial and gain mesenchymal characteristics.

One hallmark of mesenchymal cells is a greater motility than epithelial cells. To dynamically assess whether these phenotypic and molecular changes affect the behavior of mutant NNE cells we used live imaging of cranial NTC (Massarwa and Niswander, 2013). The myr-Venus reporter mouse labels all cell membranes with yellow fluorescent protein (YFP) (Rhee et al., 2006), and mating of myr-Venus:*Grhl2*$^{1Nisw/+}$ compound heterozygotes allowed us to visualize wild-type and mutant embryos by confocal microscopy (for numbers of embryos used in live imaging experiments see Table S1). Cranial NTC occurs via zippering of the neural folds moving rostrally from the cervical spinal region (closure point 1, 4-5 somites), and caudally from the anteriormost region of the future forebrain (closure point 3, 13-14 somites). Closure point 1 and initial zippering occur in *Grhl2* mutants, so we started imaging at 11 somites in the hindbrain. In wild-type embryos, zippering proceeds rostrally and the cranial folds bend towards the midline and move towards each other (Fig. 2A, Movie 1). The NNE appears tightly intact, although at the neural fold tips we observe some dynamic cell membrane movement toward the open midline, most likely filopodial extensions from the NNE (Geelen and Langman, 1979; Pyrgaki et al., 2010). We consistently observe a bright line of YFP at the neural fold tips, suggesting localized membrane constriction at the NE/NNE border (Fig. 2A, arrows). In *Grhl2* mutants, the cranial folds do not continue to elevate and ultimately fall away from each other, which in turn impedes further zippering, resulting in NTD (Fig. 2B, Movie 2). Moreover, the line of YFP at the NE/NNE border is less distinct (Fig. 2B, yellow arrows). As *Grhl2* is expressed in the NNE, not the NE or cranial mesenchyme, this implies a crucial role for the NNE in helping to shape and move the neural folds toward one another in the cranial region in mice, as has been seen in amphibians and chicks.

Grhl2$^{1Nisw/1Nisw}$ mutants fail to close the anteriormost neural folds and we noted considerable cell movement in this region in mutants (Fig. 2B, red arrow, Movie 2), prompting us to image the region of closure point 3. Here, we employed a genetic system that allows for clear distinction of the NNE. The mTmG fluorescent reporter line (Muzumdar et al., 2007) highlights all cell membranes with red fluorescent protein (mTomato) until Cre-mediated recombination results in a switch to membrane-bound green fluorescent protein (mGFP) expression. By crossing mTmG mice

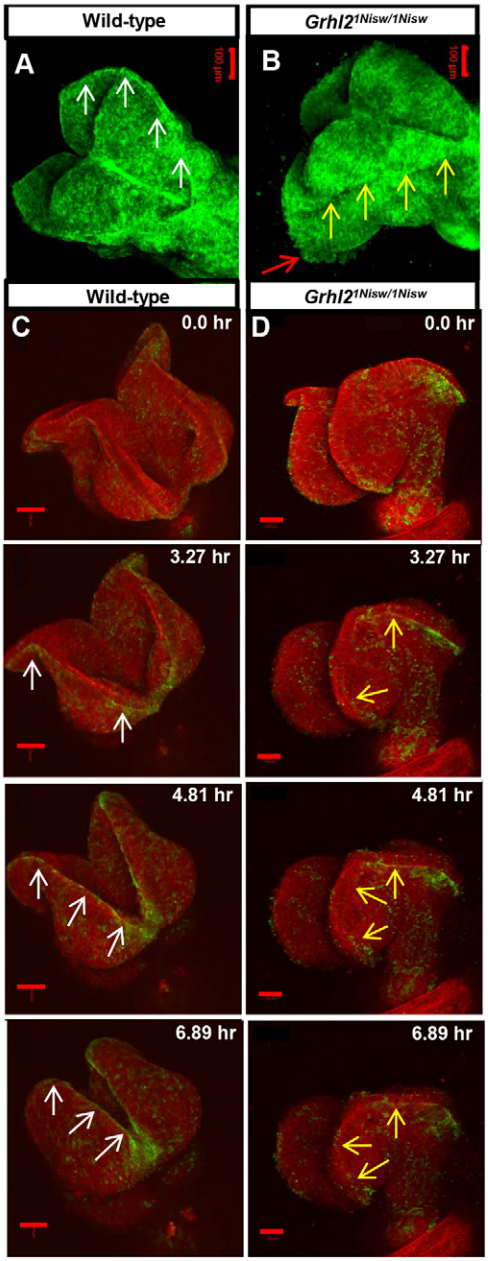

Fig. 2. Live imaging reveals dynamic alterations to NNE epithelial integrity in *Grhl2* mutants. (A,B) Still images from movies of myr-Venus wild-type and *Grhl2* mutant embryos (11 somites; dorsal view). Wild-type embryos exhibit a tight line of membrane association at the neural fold tips (A, arrows) and a smooth external epithelial surface, whereas *Grhl2* mutant embryos lack the defined membrane association (B, yellow arrows) and have a rough epithelial surface (red arrow) as the neural folds fall away. (C,D) Time series still images from live imaging of closure point 3 of mTmG:*Grhl3*$^{Cre/+}$ wild-type and *Grhl2* mutant embryos (11 somites). Wild-type NNE cells exhibit tight membrane association at the NE border (C, arrows) as the folds move toward the midline. Neural folds of *Grhl2* mutants fall away and do not meet at the midline, and the membrane association at the NNE/NE border is discontinuous and ill-defined (D, arrows). Scale bars: 100 µm.

to *Grhl3-Cre* mice, in which Cre expression is under control of the endogenous *Grhl3* promoter (Camerer et al., 2010), NNE cells at the neural fold tips are highlighted with mGFP. Crosses of mTmG:*Grhl2*$^{1Nisw/+}$ and *Grhl3-Cre*:*Grhl2*$^{1Nisw/+}$ mice allowed us to evaluate NNE behavior in both wild-type and mutant embryos. Of note, embryos carrying the *Grhl3-Cre* allele are heterozygous for

Development (2016) 143, 1192-1204 doi:10.1242/dev.129825

the wild-type *Grhl3* allele, which could genetically interact with the loss of *Grhl2*. However, at the time points examined, *Grhl2* is expressed much more broadly than *Grhl3* such that we expect the impact to be minimal.

Starting with 11-somite wild-type embryos, the opposing neural folds move toward the midline and make contact at the anteriormost point after ∼6 h of imaging (Fig. 2C, Movie 3). As the neural folds curl towards each other, the NNE at the neural fold tips displays a distinct border with the NE (mGFP, Fig. 2C, white arrows), similar to that in myr-Venus embryos. In *Grhl2* mutants, the neural folds do not move toward the midline and instead curve away from each other. mGFP expression at the NNE/NE border is indistinct and discontinuous (Fig. 2D, yellow arrows, Movie 4) and individual NNE cells display increased dynamic movement (Movie 4). Higher magnification and greatly increased speed of imaging over a 15 min timecourse revealed that wild-type NNE cells are fairly static (Movie 5). By contrast, *Grhl2* mutant NNE cells appear highly dynamic and many cells round up on the outside of the epithelium (Movie 6). Together, these data indicate that loss of GRHL2 function alters NNE epithelial integrity and results in cellular changes consistent with the molecular changes accompanying a loss of epithelial character and a gain of mesenchymal properties.

NCCs form at the NNE/NE border and, as they develop, they express a number of TFs that direct cell fate (*Sox10*) and drive their EMT [*Snail* (*Snai1*), *Zeb2*]. Analysis of these genes by *in situ* hybridization showed no global changes in expression patterns between wild-type and *Grhl2* mutant embryos, although in the mutant we occasionally noted a few cells in the NNE expressing *Snail* or *Sox10* (Fig. S1). This could be indicative of individual NNE cells expressing these TFs, or of NCCs moving into the NNE due to the loss of NNE epithelial integrity. Therefore, we evaluated NCCs more specifically by crossing *Wnt1-Cre:Grhl2*$^{1Nisw/+}$ to mTmG:*Grhl2*$^{1Nisw/+}$ to label early and migrating NCCs (Danielian et al., 1998) in wild-type and *Grhl2* mutant embryos. Transverse sections of wild-type embryos showed migrating NCC streams under the NNE layer (Fig. 3A) and an intact basement membrane containing fibronectin (Fig. 3C). In *Grhl2* mutants, some NCCs lie within the NNE layer (Fig. 3B, arrows), appearing to coincide with regions of basement membrane disruption (Fig. 3D, arrows). Dynamic imaging of wild-type embryos starting at 7 somites (dorsal view) showed NCCs within the cranial neural folds rostral of the zippering front, and chains of NCCs migrating laterally away from the midline caudal to the closed NT (Movie 7). There was no obvious overall defect in NCC migration in this region in *Grhl2* mutants (Movie 8); however, close inspection of the neural folds revealed local disruption of NCC behavior. In wild-type embryos (11 somites), NCCs arise within the neural folds bounded by the overlying NNE layer, and NCCs all move internally (Fig. 3E, arrow, Movie 9). In *Grhl2* mutants, some individual cells are seen within the NNE layer and these NCCs extend cellular processes externally (Fig. 3F, yellow arrows, Movie 10). Although our data are not conclusive, we suggest the following: while *Grhl2* loss results in increased mesenchymal properties (vimentin expression and increased cellular dynamics), the NNE does not undergo an NCC-driven EMT program, but instead the disruption in GRHL2-regulated NNE integrity fails to constrain NCCs along their migratory path under the NNE.

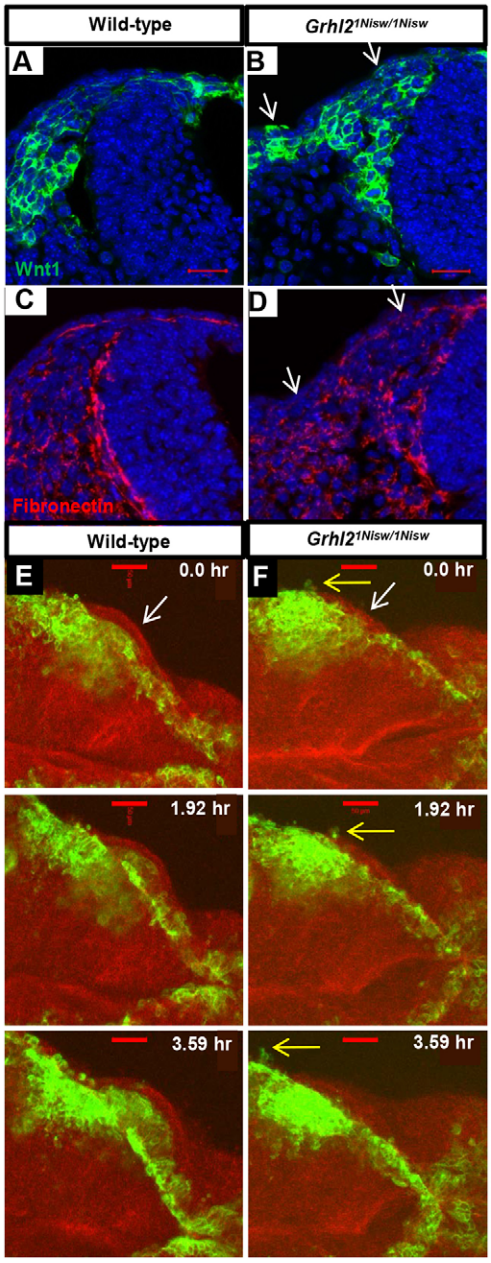

Fig. 3. Aberrant localization of migrating NCCs reflects loss of NNE epithelial integrity in *Grhl2* mutants. (A-D) Fibronectin immunostaining and NCC visualization (mTmG:*Wnt1*^{Cre}) shows NCC migration between the NE and NNE and an intact basement membrane under the NNE in wild type (A,C), whereas in *Grhl2* mutants the NNE layer contains a few NCCs and this correlates with regions of basement membrane disruption (arrows, B,D). Three embryos per genotype were analyzed. (E,F) Time series from live imaging of mTmG:*Wnt1*$^{Cre/+}$ wild-type and *Grhl2* mutant embryos (11 somites at start; dorsal view) showing NCCs at the edge of the closing neural folds and below the single layer of NNE (E,F, white arrows). In wild-type embryos, NCCs always move internally (E). In *Grhl2* mutants, a few NCCs are seen within the NNE layer and they extend cellular processes externally (F, yellow arrows). Scale bars: 20 µm in A,B; 50 µm in E,F.

Wild-type NNE expresses potential EMT suppressors

Cellular behavior of the NNE, NE and NCCs must be highly regulated in time and space for proper NTC. As these tissues adopt different characteristics (epithelial versus mesenchymal), it is conceivable that regulation of EMT, both positive and negative, plays a crucial role in NTC. Thus, we hypothesized that GRHL2 is necessary to both activate important epithelial genes and actively suppress EMT during NTC, and set out to determine if the NNE expresses EMT suppressors during NTC.

Development (2016) 143, 1192-1204 doi:10.1242/dev.129825

To isolate the NNE, we used the mTmG×*Grhl3-Cre* genetic cross to differentially label the NNE (GFP) and remaining embryonic tissue (RFP). GFP$^+$ embryos were collected (20-24 somites), dissected to remove non-NT tissue, dissociated into single-cell suspensions, and subjected to fluorescence-activated cell sorting (FACS) to isolate the NNE (GFP$^+$) and a mixed population of remaining neural and non-neural cells (RFP$^+$). RNA sequencing (RNA-seq) was performed, and subsequent Cuffdiff analysis comparing the two populations identified genes enriched in the NNE compared with the RFP$^+$ population (Table 1). Using q<0.20 and P<0.05, 48 genes were identified, including genes already characterized as NNE expressed and GRHL2 regulated [E-cadherin (*Cdh1*) and claudin 4 (*Cldn4*)], as well as genes not previously characterized in the NNE. Although GO term analysis did not identify EMT suppressors as an enriched category, an extensive literature search of all 48 genes identified six potential EMT suppressors based on work in other cell contexts (Table 1 and outlined below).

Table 1. Genes significantly enriched in NNE

Gene_id	Gene	$\log_2$ (fold-change)	*P*-value	q-value
uc007xtw.1	*Krt5*	4.22	0.002	0.200
uc009pbi.2	*Trim29*	3.39	0.002	0.182
uc007xwy.1	*Hoxc11*	3.20	<0.001	0.006
uc009cme.1	*Tlx2*	3.19	<0.001	0.026
uc007dwp.1	*Mixl1*	3.07	<0.001	0.008
uc008mno.1	*Fermt1*	2.98	<0.001	0.018
uc008ixe.1	*Dbh*	2.96	<0.001	0.013
uc007xtd.2	*Krt7*	2.93	<0.001	0.001
uc007jtb.2	*Cldn7*	2.82	0.002	0.182
uc008asw.2	*Cldn6*	2.80	<0.001	0.000
uc008kdv.1	*Hoxd12*	2.80	<0.001	0.030
uc007jlx.1	*Myh3*	2.70	<0.001	0.000
uc007clv.2	*Thsd7b*	2.69	<0.001	0.002
uc007czr.1	*Lamc2*	2.69	<0.001	0.024
uc009pio.1	*Htr3a*	2.66	<0.001	0.009
uc009iqu.1	*Art1*	2.65	0.002	0.157
uc008adl.1	*Tmprss2*	2.54	0.001	0.118
uc009kec.1	*Foxi2*	2.52	<0.001	0.020
uc008zxd.2	*Cldn4*	2.48	<0.001	0.016
uc008vgr.1	*Grhl3*	2.46	0.002	0.171
uc012dao.1	*Esrp1*	2.40	0.045	1.000
uc007njx.2	*Sostdc1*	2.39	<0.001	0.075
uc008jwu.2	*Galnt3*	2.38	<0.001	0.014
uc008kdw.1	*Hoxd11*	2.36	<0.001	0.007
uc009jqp.2	*Gsg1l*	2.31	<0.001	0.049
uc008duy.1	*Epcam*	2.19	<0.001	0.013
uc009kkl.1	*Sct*	2.18	<0.001	0.071
uc009byn.1	*Hoxa11*	2.16	0.001	0.130
uc007tbu.1	*Cdhr1*	2.16	<0.001	0.005
uc008kdx.2	*Hoxd11*	2.12	<0.001	0.007
uc009ngi.1	*Cdh1*	2.12	<0.001	0.016
uc008kdu.1	*Hoxd13*	2.04	<0.001	0.024
uc012ema.1	*Hoxa10*	2.03	<0.001	0.070
uc007bne.1	*Wnt6*	2.03	<0.001	0.038
uc007dln.1	*Rgs4*	1.97	<0.001	0.011
uc008kgt.1	*Neurod1*	1.96	<0.001	0.002
uc007xwz.1	*Hoxc10*	1.86	<0.001	0.003
uc009tzk.1	*Cdx4*	1.80	<0.001	0.010
uc008ajq.1	*T*	1.74	<0.001	0.008
uc007crl.2	*Myog*	1.66	0.002	0.153
uc007mfq.1	*Kif19a*	1.63	0.001	0.112
uc007nau.1	*Msgn1*	1.63	0.001	0.135
uc009anz.1	*Cdx2*	1.56	<0.001	0.097
uc007vne.2	*Grhl2*	1.41	0.006	1.000
uc008tuv.1	*Foxd3*	1.40	<0.001	0.097
uc007hnm.1	*Erbb3*	1.26	<0.001	0.079
uc007wsu.2	*Sox10*	1.25	<0.001	0.015
uc007ulo.1	*Nefm*	1.11	0.001	0.139

RNA-seq of FACS-sorted GFP$^+$ cells (NNE) and RFP$^+$ cells (neural and remaining embryonic tissue) from 20- to 24-somite embryos from mTmG×*Grhl3-Cre* cross. Table shows genes (gene_id refers to the UCSC Genome Bowser gene identifier; gene symbol from Mouse Genome Informatics) enriched in the NNE relative to the remaining embryonic tissue.

Epithelial splicing regulatory protein 1 (ESRP1, also known as RBM35A) is expressed in epithelial tissues, promotes epithelial-specific splicing of many genes, and was identified as an EMT suppressor in the context of breast cancer (Warzecha et al., 2010, 2009). Sclerostin domain-containing protein 1 (SOSTDC1, also known as WISE, USAG-1, ectodin) is a secreted protein that regulates tooth development (Kassai et al., 2005). SOSTDC1 inhibits BMP signaling (Kiso et al., 2014; Laurikkala et al., 2003) and, depending on the context, can activate or inhibit WNT signaling (Itasaki, 2003). BMP and WNT signaling can regulate EMT (Lim and Thiery, 2012; Micalizzi and Ford, 2009), and both are involved in NNE, NE and NCC specification (Steventon et al., 2005). Fermitin family homolog 1 (FERMT1, also known as kindlin-1) is a focal adhesion protein involved in integrin activation, adhesion of keratinocytes to fibronectin and laminin, wound healing, and EMT regulation in breast cancer cells, and *FERMT1* mutations result in Kindler syndrome, which is characterized by skin blistering (Larjava et al., 2008; Siegel et al., 2003; Ussar et al., 2008; Sin et al., 2011). Tripartite motif-containing 29 (TRIM29, also known as ATDC) is tumor promoting or suppressive depending on the context, and acts as an EMT suppressor in breast cancer (Ai et al., 2014; Liu et al., 2012). Transmembrane protease serine 2 (TMPRSS2, also known as epitheliasin) is highly expressed in prostate and is involved in EMT regulation in prostate cancer metastasis (Lucas et al., 2014). Laminin gamma 2 (LAMC2) is an epithelial-specific isoform that is highly expressed in many embryonic tissues and adult skin, kidneys and lung, and is found at low levels in a highly invasive prostate cancer cell line (Aumailley and Smyth, 1998; Copp et al., 2011; Drake et al., 2010). LAMC2 helps anchor epithelial cells to the basement membrane (Pulkkinen et al., 1994) and its expression is directly inhibited by the EMT-inducing TF ZEB1 (Drake et al., 2010). These six genes were chosen to explore their relationship with GRHL2 during NT closure and whether each, individually, can repress EMT and help promote epithelial fate.

Expression of potential EMT suppressors is altered in *Grhl2$^{1Nisw/1Nisw}$* embryos

As GRHL2 is an important TF within the NNE, we first determined whether expression of these six genes is altered in *Grhl2* mutant embryos. qRT-PCR analysis of cranial tissue showed that all six genes are downregulated in *Grhl2$^{1Nisw/1Nisw}$* relative to wild-type embryos (Fig. 4A). Whole-mount RNA *in situ* hybridization (17- to 18-somite embryos) showed altered gene expression patterns in *Grhl2* mutant embryos in tissues in which *Grhl2* is expressed (NNE, branchial arches) but not in tissues that are not GRHL2 regulated (gut endoderm) (Fig. S2). As gene expression within the single-cell layer of the NNE is difficult to see in whole-mount, we performed *in situ* hybridization on transverse sections to more specifically analyze expression. *Fermt1*, *Trim29*, *Tmprss2* and *Lamc2* expression was decreased within the mutant NNE along the length of the cranial neural folds, whereas *Esrp1* was decreased only near the fold tip (Fig. 4B). *Sostdc1* expression was not apparently affected, suggesting additional mechanisms for *Sostdc1* regulation beyond GRHL2.

Development (2016) 143, 1192-1204 doi:10.1242/dev.129825

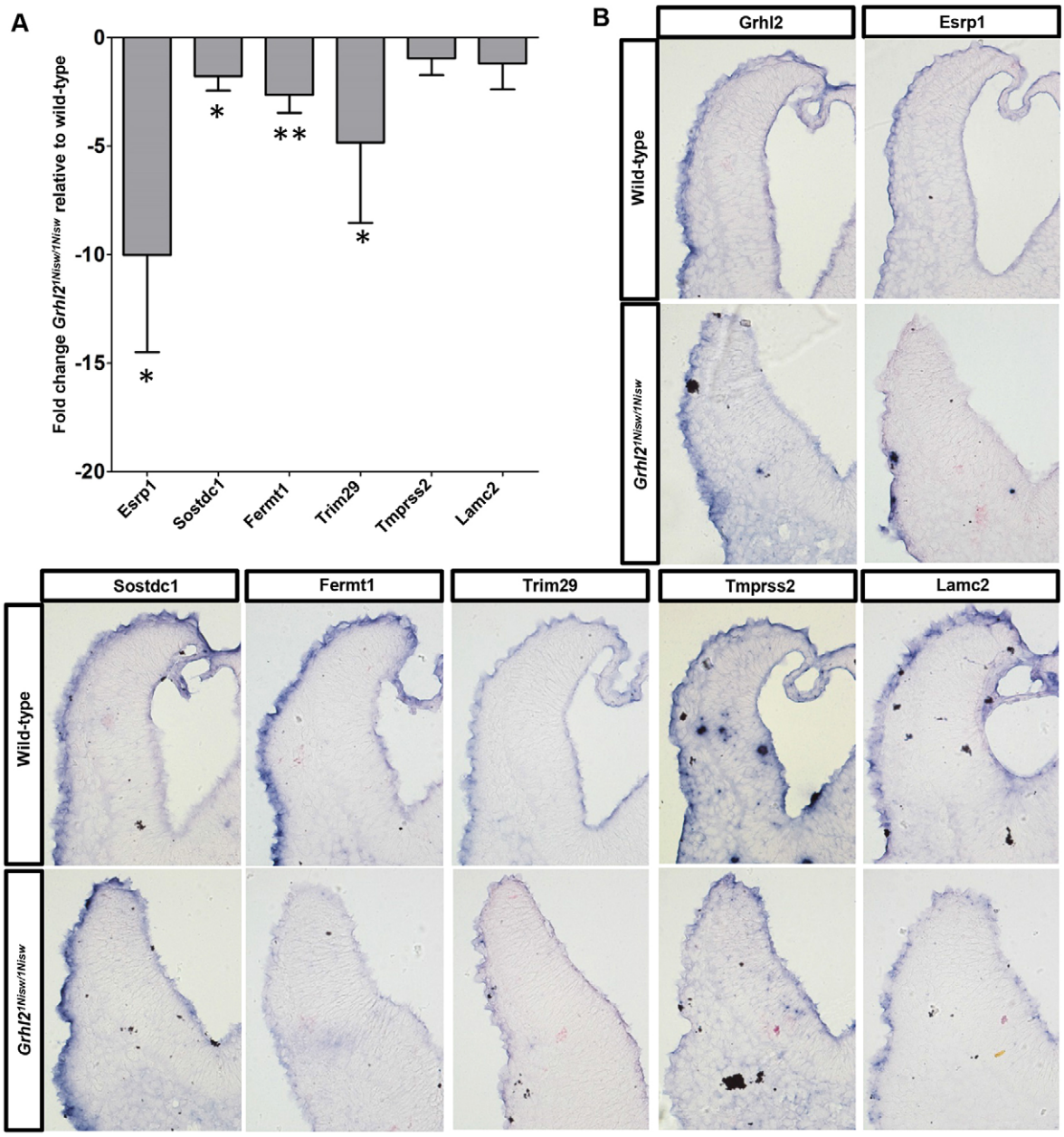

Fig. 4. *Esrp1*, *Sostdc1*, *Fermt1*, *Trim29*, *Tmprss2* and *Lamc2* expression is reduced in *Grhl2* mutant embryos. (A) qRT-PCR analysis shows decreased expression of NNE genes in *Grhl2* mutant versus wild-type embryos. Experiments were performed in biological quadruplicate with technical quintuplicates. Mean±s.d. **P*<0.05, ***P*<0.01, Student's *t*-test. (B) *In situ* hybridization of transverse sections of cranial neural folds shows altered expression of *Esrp1*, *Fermt1*, *Trim29*, *Tmprss2* and *Lamc2* in *Grhl2* mutant NNE. Four embryos per genotype were analyzed in separate technical replicates.

GRHL2 directly regulates transcription in the NNE and thus it is possible that GRHL2 directly activates these six genes. A comprehensive list of GRHL2-regulated genes in the NNE has yet to be determined, but several recent ChIP-seq studies in other tissues have identified genetic regions that are bound by GRHL2 (Aue et al., 2015; Gao et al., 2013; Walentin et al., 2015), including within the regulatory regions of *Esrp1*, *Trim29*, *Sostdc1*, *Fermt1* and *Lamc2*. Although no data were found for *Tmprss2*, interrogation using the published GRHL2 binding motif (Werth et al., 2010) identified potential GRHL2 binding sites within the regulatory regions of *Tmprss2*. Together, these data suggest that GRHL2 activates *Esrp1*, *Sostdc1*, *Fermt2*, *Trim29*, *Tmprss2* and *Lamc2* in the NNE through direct DNA binding and transcriptional activation.

Esrp1, *Sostdc1*, *Fermt1*, *Tmprss2* and *Lamc2* regulate EMT *in vitro*

To assess possible EMT function of the identified genes we utilized the IMCD-3 (mouse intermedullary collecting duct cells) cell line, which expresses high levels of GRHL2 and has been used previously to characterize GRHL2 activity (Werth et al., 2010). qRT-PCR analysis showed that *Trim29* is not expressed in IMCD-3 cells, but *Esrp1*, *Fermt1* and *Tmprss2* are expressed at even higher levels than E-cadherin and *Grhl2* (Fig. 5A). Knockdown (KD) of *Grhl2* by stable expression of an shRNA causes IMCD-3 cells (shGrhl2) to exhibit a more mesenchymal appearance, versus the 'cobblestone' epithelial morphology observed after 'KD' with stably expressed control shRNA (shControl cells) (Fig. 5B), similar

Development (2016) 143, 1192-1204 doi:10.1242/dev.129825

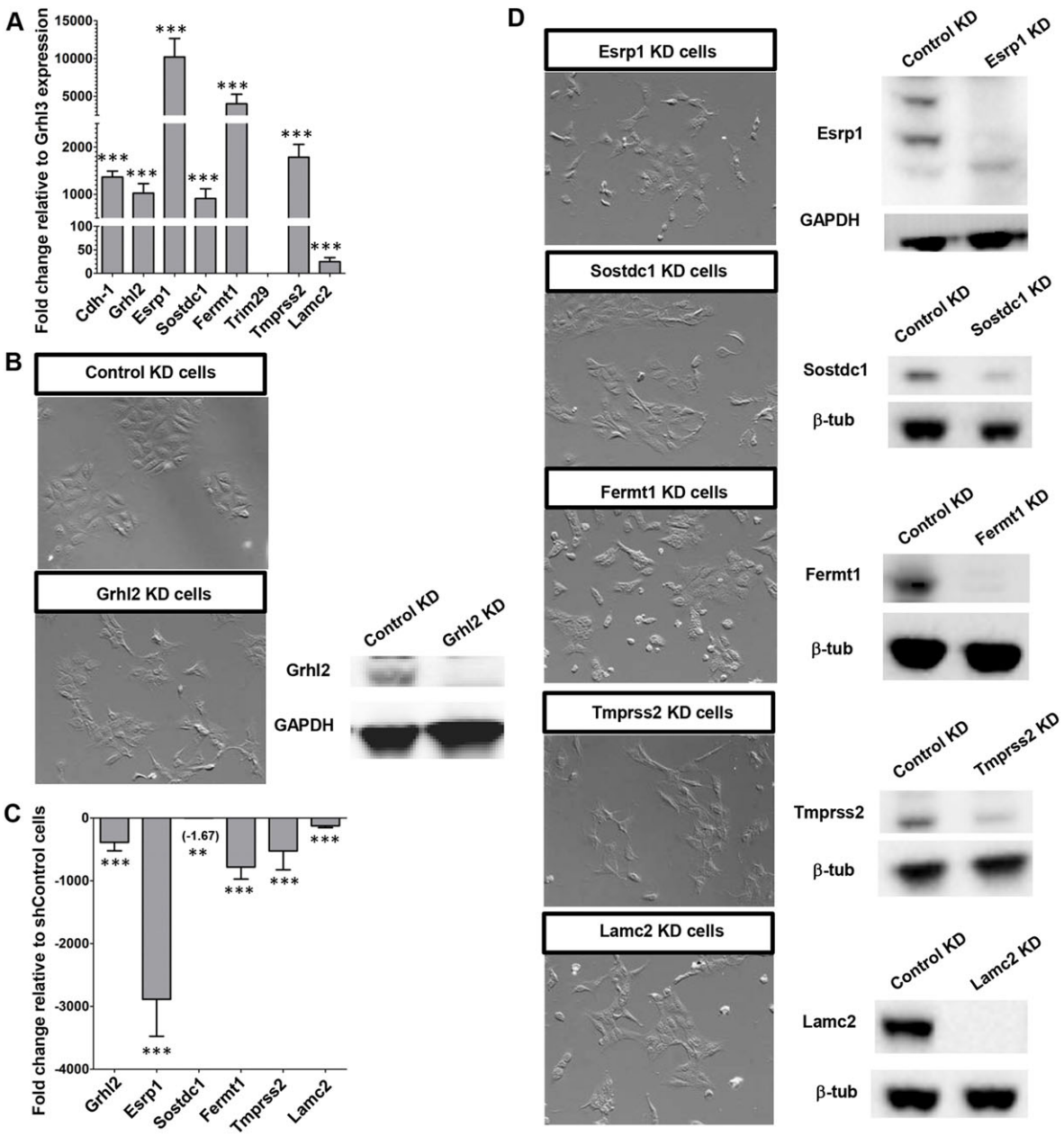

Fig. 5. Loss of *Grhl2*, *Esrp1*, *Sostdc1*, *Fermt1*, *Tmprss2* or *Lamc2 in vitro* results in a mesenchymal phenotype. (A) qRT-PCR analysis of RNA from IMCD-3 cells shows strong expression of *Grhl2* and its targets relative to *Grhl3*. (B,C) Control KD IMCD-3 (shControl) cells have an epithelial cobblestone morphology, whereas *Grhl2* KD (shGrhl2) cells appear mesenchymal and show a significant decrease in expression levels of *Grhl2* and its targets as assessed by qRT-PCR. (A,C) Experiments were performed in biological quadruplicate with technical quintuplicates. Mean±s.d. ***P*<0.01, ****P*<0.001, Student's *t*-test. (D) Cells subject to individual gene KD for *Esrp1*, *Sostdc1*, *Fermt1*, *Tmprss2* or *Lamc2* exhibit a mesenchymal morphology.

to previous results (Werth et al., 2010). As in *Grhl2* mutant embryos, *Esrp1*, *Fermt1*, *Tmprss2* and *Lamc2* are downregulated in shGrhl2 compared with shControl cells (Fig. 5C). *Sostdc1* showed the smallest fold change in expression (−1.67 fold), consistent with our *in situ* data suggesting that *Sostdc1* may be regulated by mechanisms that act in conjunction with GRHL2.

Cell lines were generated that stably express shRNAs individually targeting *Esrp1*, *Sostdc1*, *Fermt1*, *Tmprss2* or *Lamc2* (Fig. 5D). Similar to shGrhl2, cells of each KD cell line are more spindle-like and do not tightly associate with neighboring cells when in contact, indicative of EMT. IMCD-3 shControl cells express ZO-1 at cell-cell junctions and do not express vimentin (Fig. 6A). In shGrhl2 cells, ZO-1 is expressed in a jagged pattern, indicating that the connections between cells are not uniform. Strikingly, shGrhl2 cells express high levels of vimentin, a well-known marker of post-EMT cells, which also highlights the change to a mesenchymal shape (Fig. 6B). Stable shRNA KD of each of the five genes showed a pattern of ZO-1 and vimentin expression similar to that of shGrhl2 cells (Fig. 6C,E-G), with some slight differences in individual cell phenotypes.

Another characteristic of EMT is a switch from E-cadherin to N-cadherin (cadherin 2) expression. shControl cells exclusively express E-cadherin at their cell-cell junctions (Fig. 6H), whereas shGrhl2, shEsrp1, shFermt1, shTmprss2 and shLamc2 cells switch to N-cadherin junctional expression (Fig. 6I,J,L-N). shSostdc1 cells at low density appear mesenchymal, with individual scattered cells

Development (2016) 143, 1192-1204 doi:10.1242/dev.129825

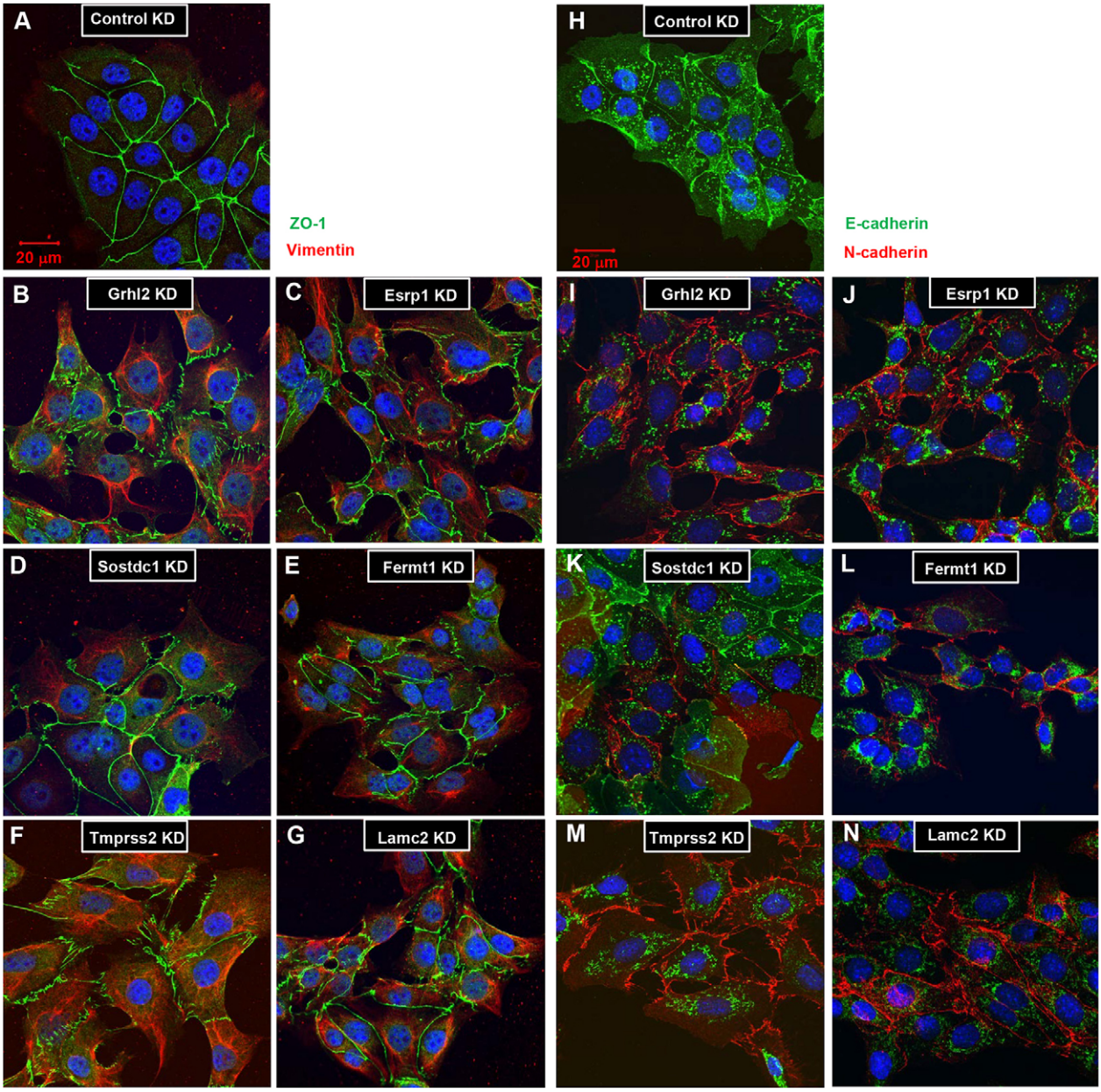

Fig. 6. Loss of *Grhl2*, *Esrp1*, *Sostdc1*, *Fermt1*, *Tmprss2* or *Lamc2* expression in IMCD-3 cells causes altered protein expression indicative of an EMT. Immunofluorescence for ZO-1 and vimentin (A-G) or E-cadherin and N-cadherin (H-N) on stable KD cell lines. (A) shControl cells exhibit a highly regular pattern of ZO-1 at the tight junctions between cells, and do not express vimentin. (B) shGrhl2, (C) shEsrp1, (D) shSostdc1, (E) shFermt1, (F) shTmprss2 and (G) shLamc2 cells all show irregular ZO-1 and aberrant vimentin expression patterns. (H) shControl cells exclusively express E-cadherin at the adherens junctions. (I) shGrhl2, (J) shEsrp1, (K) shSostdc1, (L) shFermt1, (M) shTmprss2 and (N) shLamc2 cells all show a switch from E-cadherin to N-cadherin expression. Experiments were performed in triplicate. Scale bars: 20 µm.

and vimentin expression. However, as cell density increases, forcing the cells into contact, the cells re-establish a more epithelial appearance and colony morphology. Some shSostdc1 cells exhibit an epithelial ZO-1 expression pattern, whereas others retain vimentin expression (Fig. 6D), and cadherin expression is mixed (Fig. 6K). Although these changes in shSostdc1 cell identity might be due to the intrinsic properties of SOSTDC1, the fact that SOSTDC1 functions as a modulator of BMP and WNT signaling suggests that signaling through both pathways might be required to push cells into a full EMT. These experiments show that individual loss of *Grhl2*, *Esrp1*, *Sostdc1*, *Fermt1*, *Tmprss2* or *Lamc2* expression is sufficient to induce a phenotypic and molecular EMT.

Other hallmarks of EMT are an increase in cellular motility and invasion through a basement membrane. To assess a functional EMT, we measured the ability of KD cells to migrate through a Transwell filter toward a chemoattractant. A small number of shControl epithelial cells can migrate through the filter pores but shGrhl2 cells migrate in significantly greater numbers (Fig. 7A,B), consistent with a role for GRHL2 as a tumor suppressor (Cieply et al., 2012). *Tmprss2* KD (shTmprss2) causes significantly greater migration than seen in shControl cells, and shEsrp1, shFermt1 and shLamc2 cells show greater migration than even shGrhl2 cells (Fig. 7A,B). Invasiveness was assessed by the ability to migrate through the filter in the presence of basement membrane. shGrhl2

Development (2016) 143, 1192-1204 doi:10.1242/dev.129825

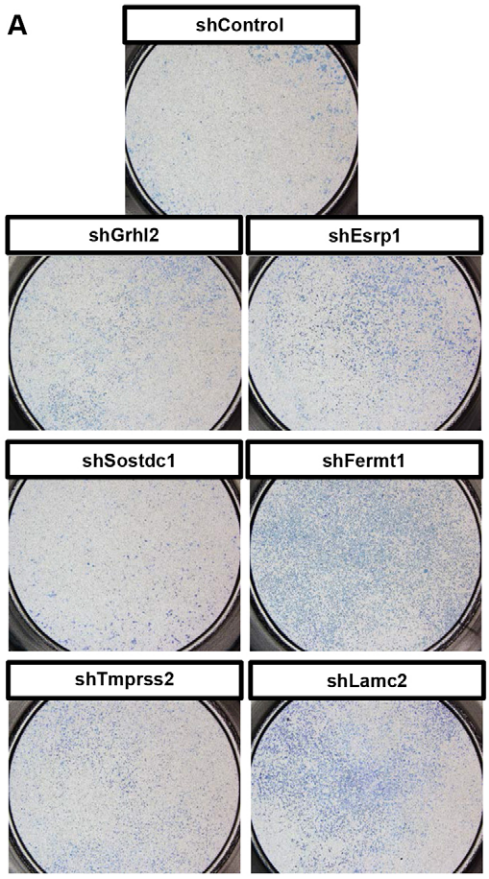

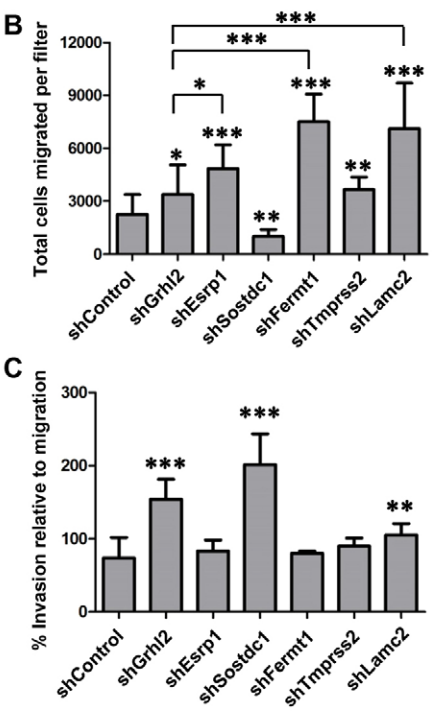

Fig. 7. *Grhl2*, *Esrp1*, *Sostdc1*, *Fermt1*, *Tmprss2* and *Lamc2* KD cells undergo a functional EMT. (A) Images of whole Transwell filters seeded with IMCD-3 cells in which the specified genes have been subject to KD by shRNA, showing their differential ability to migrate toward a chemoattractant. (B) Quantification of A. (C) Quantification of the total number of KD cells that invaded through a basement membrane relative to migration through the filter alone. Experiments were performed in biological and technical triplicate. Mean±s.d. **P*<0.05, ***P*<0.01, ****P*<0.001, Student's *t*-test.

cells show a significantly greater invasive phenotype than shControl cells (Fig. 7C). Interestingly, shSostdc1 cells showed a highly invasive phenotype, although their migratory ability was reduced relative to the control (Fig. 7B,C). Altogether, these data show that KD of *Esrp1*, *Sostdc1*, *Fermt1*, *Tmprss2* or *Lamc2* each results in a functional EMT, although the differences between the cell lines in phenotype, migratory and invasive capacity suggest that each gene might regulate different aspects of the EMT program. These results support the hypothesis that GRHL2 actively regulates EMT within the NNE during NTC through the activation of the downstream EMT suppressors *Esrp1*, *Sostdc1*, *Fermt1*, *Tmprss2* and *Lamc2*.

DISCUSSION

NTDs constitute one of the most prevalent classes of birth defects worldwide. Genetic studies in mouse have been instrumental in teasing apart the genetic basis of NTC, with over 300 mouse NTD models (Harris and Juriloff, 2010). The majority of these mouse mutants exhibit cranial NTDs, and mechanistic studies have increased an understanding of the cellular processes necessary for cranial NTC, including regulation of the actin cytoskeleton (Hildebrand and Soriano, 1999; Morriss-Kay and Tuckett, 1985; Xu et al., 1998), neuroepithelial cell proliferation (Honarpour et al., 2001; Ishibashi et al., 1995; Lardelli et al., 1996), neural patterning (Copp and Greene, 2013; Huangfu et al., 2003), apoptosis (Cecconi et al., 1998; Leonard et al., 2002; Yamaguchi et al., 2011) and NCC emigration (Yamaguchi and Miura, 2013). Most studies have focused on the NE, whereas much less is known about how the NNE contributes to NTC. As *Grhl2* is expressed exclusively in the NNE during NTC, and loss of GRHL2 function results in fully penetrant cranial NTDs, *Grhl2* mutants offer a unique opportunity to study the role of the NNE in cranial NTC.

Here we found that loss of *Grhl2* expression alters the epithelial integrity of the NNE, and that GRHL2 normally functions not only through the activation of downstream epithelial genes but also through the active suppression of EMT. Our studies provide the first transcriptome analysis of wild-type NNE and we identified five genes downstream of GRHL2 that act as EMT suppressors in epithelial cells. Loss of *Grhl2* causes NNE disruption, including disorganized cell junctions, aberrant expression of the mesenchymal protein vimentin, and decreased epithelial integrity. Live imaging showed that the sharp border between NE and NNE is disrupted and individual NNE cells are more dynamic, with some leaving the epithelial layer. *Grhl2* mutant cranial neural folds are initially able to elevate, but they do not continue to move toward the midline and instead fall away from each other.

It appears that the major cause of NTD in *Grhl2*$^{1Nisw/1Nisw}$ embryos is the loss of NNE integrity. We speculate that this may lessen the force applied by the NNE against the underlying mesenchyme and NE to help push the neural folds together, although we cannot rule out other potential GRHL2-regulated processes. The forces involved in murine NTC have not been experimentally determined, but studies in other model organisms support this hypothesis. During chick cranial NTC, NNE removal does not affect initial neural fold elevation but the folds are unable to fully elevate and fail to converge toward the midline (Hackett et al., 1997). Moreover, it has been proposed that NNE cells preferentially expand in the medial direction and push against the underlying ECM to generate force to bring the neural folds together (Moury and Schoenwolf, 1995). In *Xenopus laevis*, the NNE is held under

Development (2016) 143, 1192-1204 doi:10.1242/dev.129825

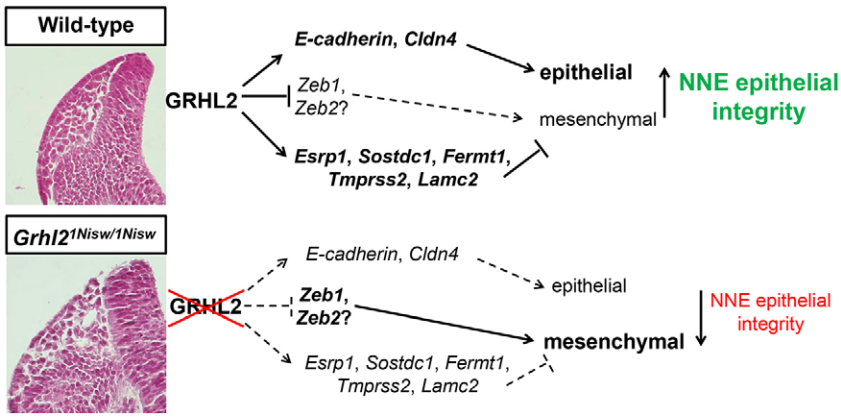

Fig. 8. Model for GRHL2 regulation of epithelial integrity in NNE. GRHL2 regulates integrity of the NNE through activation of epithelial junctional proteins, direct suppression of ZEB TFs, and activation of several EMT suppressors to enforce the epithelial phenotype of NNE. GRHL2 loss shifts the NNE properties, resulting in loss of epithelial and gain of mesenchymal characteristics.

directional tensile forces that contribute to tissue movement, and disruption of the morphogenetic movement of the NNE results in failure of NTC (Morita et al., 2012). *Grhl2*$^{1Nisw/1Nisw}$ mutants show only cranial NTD, although *Grhl2* is also expressed in the spinal region. The mechanism underlying this differential phenotype is unclear. We hypothesize that the cranial NTD relates to differences in morphogenetic movements of the neural folds in the cranial region, which span a much greater distance than the spinal neural folds, thus perhaps requiring a greater contribution of the NNE to help move the cranial neural folds together. Indeed, we showed here that NNE integrity in *Grhl2* mutant rostral spinal cord is also disrupted but that the spinal neural folds are able to meet and seal at the midline. Although we have not tested our hypothesis experimentally, the proposed mechanism could explain why the cranial folds are more sensitive to disruption of the NNE. Thus, we suggest that GRHL2 function is required throughout the cranial NNE to maintain the tissue structure necessary for appropriate bending and movement of the cranial neural folds toward one another.

As the neural folds approach one another, extensive tissue remodeling is required to separate the NE and NNE to allow new connections with the partner tissue on the opposing folds. Scanning electron microscopy and live imaging studies show that cellular projections emanate from the NNE towards the midline that may contribute to NTC (Geelen and Langman, 1979; Pyrgaki et al., 2010). Meanwhile, the NCCs delaminate from the epithelium at the NE/NNE border to migrate away, and our live imaging provides insight into NCC dynamics in the mouse embryo. It is currently unknown how remodeling of the neural folds occurs, but one can imagine that the NE and NNE cells must alter their adhesive, epithelial properties to release from each other. Also, NNE cells just at the tips alter their behavior to promote cellular extensions that project toward the dorsal midline. Thus, we propose the following model for how GRHL2 expression enforces NNE epithelial integrity, even during epithelial remodeling and NCC EMT (Fig. 8). During closure of the cranial neural folds, *Grhl2* is expressed throughout the NNE. GRHL2 directly activates epithelial junctional proteins, such as E-cadherin and claudin 3/4 (Mostov et al., 2012; Werth et al., 2010), and activates expression of the EMT suppressor proteins ESRP1, SOSTDC1, FERMT1, TMPRSS2 and LAMC2. Concordantly, GRHL2 directly represses *Zeb1* (Cieply et al., 2012) and possibly the NCC-expressed *Zeb2*. Together, this GRHL2-mediated gene regulatory network enforces the epithelial properties of the NNE during this period of extensive tissue remodeling.

EMT reflects a complex series of events in which epithelial cells lose their apicobasal polarity, decrease cell-cell adhesions, disrupt their interaction with the basement membrane, undergo cytoskeletal rearrangement including the generation of lamellipodia and filopodia, and become migratory (Lim and Thiery, 2012; Micalizzi and Ford, 2009). These changes are governed by extracellular signaling, transcriptional regulation, alternative splicing and miRNA expression. Thus, suppression of EMT requires multiple mechanisms working in concert. Here we characterized five GRHL2-regulated genes in the NNE that act as EMT suppressors, each of which might impact different aspects of the EMT program. We identified genes that affect signaling pathways (*Sostdc1*, *Tmprss2*), alter isoform expression from pro-mesenchymal to pro-epithelial (*Esrp1*), and are involved in cell-ECM interactions (*Fermt1*, *Lamc2*). Individual KD of each gene *in vitro* shows EMT and similar gross changes in protein expression indicating that they are EMT suppressors. However, fine differences can be appreciated in cell interactions, protein expression, and functional studies of migration and invasion. This suggests that these genes act in combination to fully suppress EMT and that GRHL2 ensures that the NNE remains epithelial through targeting multiple aspects of EMT. To our knowledge, this is the first characterization of GRHL2 as an EMT suppressor during development, and ChIP-seq studies in other systems (Gao et al., 2013; Walentin et al., 2015) reveal that GRHL2 binds to the regulatory regions of the majority of these genes during lung and placental development. This suggests a general mechanism during the development of epithelial tissues, whereby activation of epithelial-specific genes is accompanied by the active suppression of EMT pathways to ensure rapid and robust epithelial morphogenesis.

Genes that normally regulate development are often altered in cancer cells and EMT is a necessary step leading to metastasis. This begs the question: can we use developmental systems of EMT suppression to identify new EMT suppressors in the context of cancer and potential new therapeutic targets? Several genes studied here and additional genes identified in the RNA-seq show promise as EMT suppressors through the mining of publicly available databases of human tumors. Studies are currently underway to assess the potential of these genes to suppress both the EMT process itself and metastasis during *in vivo* tumorigenesis.

MATERIALS AND METHODS

Mice

Grhl2^{1Nisw} mice were generated through ENU mutagenesis (Pyrgaki et al., 2011) and maintained as heterozygous animals (Jackson Laboratory stock #016156). For live embryo imaging, the following transgenic mice were used: mTomato:mGFP [Jackson Laboratory #007576 (Muzumdar et al., 2007)], pCAG::myr-Venus [Jackson Laboratory #011107 (Rhee et al.,

Development (2016) 143, 1192-1204 doi:10.1242/dev.129825

2006)], *Grhl3-Cre* (Camerer et al., 2010) and *Wnt1-Cre* (Danielian et al., 1998). Male breeder mice were used within 1 year of age and all female mice were mated between 6 and 16 weeks of age. Mice were housed at the University of Colorado Anschutz Medical Campus in accordance with IACUC approved protocol.

Cell culture

The IMCD-3 cell line (a generous gift of Dr Christopher Rivard at UCDAMC) was cultured in DMEM/F12 and 10% FBS. Cells were transfected with shRNA plasmids using Lipofectamine 2000 (Thermo Scientific) followed by puromycin selection to generate clonal populations with stable shRNA integration. shRNA plasmids were obtained from the MISSION TRC1 shRNA plasmid bank at University of Colorado Boulder (Sigma): Grhl2-NM_026496.1-814s1c1, Esrp1-NM_194055.1-929s1c1, Fermt1-NM_198029.1-660s1c1, Sostdc1-NM_025312.1-419s1c1, Tmprss2-NM_015775.2-2761s1c1, Lamc2-NM_008485.2-4335s1c1.

Immunohistochemistry and western blots

Protocols for immunostaining of tissue cryosections and cell lines, including details of antibodies and stains and quantification using Imaris software (Bitplane), are provided in Table S2 and legend.

Histology and *in situ* hybridization

Whole-mount and section *in situ* hybridization were performed as described (Holmes and Niswander, 2001; Liu et al., 1998) using probes generated from cDNA made from embryonic mouse total RNA with the primer pairs listed in Table S3. Hematoxylin and Eosin (H&E) staining employed standard methods. For further details see Table S3 and legend.

Whole-embryo culture and time-lapse microscopy

Embryos were dissected at E8.5, mounted and imaged as described (Massarwa and Niswander, 2013). For high-speed imaging, 11-somite embryos were imaged every 15 s for 15 min total on a Zeiss 5 Live confocal microscope system with images acquired using a Plan-Achromat 10×/0.45 objective at 2.0× magnification.

RNA-seq

mTmG homozygous females were mated to *Grhl3-Cre* males, embryos dissected at E9.5 in Tyrode's buffer, GFP^+ embryos selected and dissected further to remove the brachial arch regions, heart and gut endoderm, then pooled according to somite stage. Tissue was placed in Hanks' Balanced Salt Solution without calcium and magnesium (HBSS-free, Gibco 14175) and centrifuged at 1000 rpm (100 ***g***) for 4 min. HBSS was aspirated, 100 µl of dissociation medium (800 µl HBSS-free, 100 µl collagenase IV, 100 µl 0.25% trypsin/EDTA) was added and the sample incubated at 37°C for 4 min. Then 7.5 µg DNase in FACS staining medium [132 ml L15 medium without Phenol Red (Gibco), 1% pen/strep (10,000 U/ml), 1 mg/ml BSA, 10 mM HEPES pH 7.4, 10% water] was added and the sample immediately centrifuged at 1000 rpm (100 ***g***) for 4 min followed by medium aspiration. Cells were dissociated in 1 ml FACS staining medium by gentle pipetting followed by passage through a 0.45 µm cell filter. Cells were sorted into GFP^+ and $Tomato^+$ pools using a MoFlo XDP 100 cell sorter (UC Cancer Center, Flow Cytometry Shared Resource) and immediately processed using the Arcturus PicoPure RNA Isolation Kit (Applied Biosystems). RNA libraries were prepared from 1 µg RNA using the TruSeq RNA Sample Preparation Kit (Illumina) and high-throughput RNA sequencing performed using an Illumina HiSeq 2000 sequencer (Dr Jim Huntley, UC Boulder) to generate 1×100 reads. Data were analyzed by Dr Jay Hesselberth (UC Denver AMC) for NNE-specific gene expression (GFP^+) in comparison to remaining tissue ($Tomato^+$) using Bowtie/TopHat and Cufflinks analysis software (Roberts et al., 2012). Significant differences in gene expression were determined by $q<0.20$ and $P<0.05$. The complete RNA-seq dataset is available at GEO (accession number GSE72059).

Real-time PCR

E9.5 heads were isolated by dissecting above the first brachial arch dorsally to the otic vesicle, and tissue was snap frozen. RNA from $Grhl2^{+/+}$ and $Grhl2^{1Nisw/1Nisw}$ embryos was isolated from individual samples and cDNA generated from 350 ng total RNA using the Superscript III Reverse Transcription Kit (Invitrogen). cDNA from cell lines was prepared from 2 µg total RNA. Quantitative real-time PCR (qRT-PCR) was performed on a Roche LC480 thermocycler using either TaqMan probes or the Universal Probe Library system (UPL, Roche Diagnostics) with *Gapdh* as endogenous control. Fold changes in gene expression were calculated based on the ΔΔCT method of relative quantitation. All experiments were performed in biological quadruplicate with technical quintuplicates and statistical analysis was performed using the two-tailed Student's *t*-test.

Migration and invasion assays

Cells were plated in 10 cm dishes, incubated for 2 days until ∼75% confluency and serum starved for 24 h. Cells were dissociated with HyQtase (Hyclone), spun down and resuspended in serum-free medium. Using a modified Boyden chamber assay, 2.5×10^4 cells were seeded in a Transwell permeable support (8 µm pore size, Corning) with or without basement membrane extract (BME, Trevigen), and medium with 10% FBS added into the bottom chamber as a chemoattractant. After 24 h, filters were fixed and stained using the Diff-Quick Staining Kit per protocol (Thermo Fisher), imaged and total cell numbers counted. Assays were performed in technical and biological triplicate and the two-tailed Student's *t*-test used for statistical analysis.

Acknowledgements

We thank Drs Jim Huntley and Jay Hesselberth for RNA-seq and data analysis, the UC Cancer Center Flow Cytometry Core for FACS sorting, and Dr Trevor Williams for the *Esrp1 in situ* probe.

Competing interests

The authors declare no competing or financial interests.

Author contributions

H.J.R. and L.A.N. contributed to experimental design, data analysis and manuscript preparation; H.J.R. performed all experiments.

Funding

L.A.N. was an Investigator of the Howard Hughes Medical Institute. This work was supported by the National Institutes of Health [1F31CA180438-01 to H.J.R.]; Cancer League of Colorado; and UC Cancer Center. Deposited in PMC for release after 6 months.

Data availability

The complete RNA-seq dataset is available at Gene Expression Omnibus with accession number GSE72059.

Supplementary information

Supplementary information available online at
http://dev.biologists.org/lookup/suppl/doi:10.1242/dev.129825/-/DC1

References

Ai, L., Kim, W.-J., Alpay, M., Tang, M., Pardo, C. E., Hatakeyama, S., May, W. S., Kladde, M. P., Heldermon, C. D., Siegel, E. M. et al. (2014). TRIM29 suppresses TWIST1 and invasive breast cancer behavior. *Cancer Res.* **74**, 4875-4887.

Aue, A., Hinze, C., Walentin, K., Ruffert, J., Yurtdas, Y., Werth, M., Chen, W., Rabien, A., Kilic, E., Schulzke, J.-D. et al. (2015). A Grainyhead-Like 2/Ovo-Like 2 pathway regulates renal epithelial barrier function and lumen expansion. *J. Am. Soc. Nephrol.* **26**, 2704-2715.

Aumailley, M. and Smyth, N. (1998). The role of laminins in basement membrane function. *J. Anat.* **193**, 1-21.

Camerer, E., Barker, A., Duong, D. N., Ganesan, R., Kataoka, H., Cornelissen, I., Darragh, M. R., Hussain, A., Zheng, Y.-W., Srinivasan, Y. et al. (2010). Local protease signaling contributes to neural tube closure in the mouse embryo. *Dev. Cell* **18**, 25-38.

Cecconi, F., Alvarez-Bolado, G., Meyer, B. I., Roth, K. A. and Gruss, P. (1998). Apaf1 (CED-4 homolog) regulates programmed cell death in mammalian development. *Cell* **94**, 727-737.

Chen, W., Liu, Z., Oh, J.-E., Shin, K., Kim, R. H., Jiang, M., Park, N.-H. and Kang, M. K. (2012). Grainyhead-like 2 (GRHL2) inhibits keratinocyte differentiation through epigenetic mechanism. *Cell Death Dis.* **3**, e450.

Cieply, B., Riley, P., Pifer, P. M., Widmeyer, J., Addison, J. B., von Ivanov, A., Denvir, J. and Frisch, S. M. (2012). Suppression of the epithelial-mesenchymal transition by Grainyhead-like-2. *Cancer Res.* **72**, 2440-2453.

Development (2016) 143, 1192-1204 doi:10.1242/dev.129825

Cieply, B., Farris, J., Denvir, J., Ford, H. L. and Frisch, S. M. (2013). Epithelial-mesenchymal transition and tumor suppression are controlled by a reciprocal feedback loop between ZEB1 and Grainyhead-like-2. *Cancer Res.* **73**, 6299-6309.

Copp, A. J. and Greene, N. D. E. (2013). Neural tube defects-disorders of neurulation and related embryonic processes. *Wiley Interdiscip. Rev. Dev. Biol.* **2**, 213-227.

Copp, A. J., Brook, F. A., Estibeiro, J. P., Shum, A. S. W. and Cockroft, D. L. (1990). The embryonic development of mammalian neural tube defects. *Prog. Neurobiol.* **35**, 363-403.

Copp, A. J., Greene, N. D. and Murdoch, J. N. (2003). The genetic basis of mammalian neurulation. *Nat. Rev. Genet.* **4**, 784-793.

Copp, A. J., Carvalho, R., Wallace, A., Sorokin, L., Sasaki, T., Greene, N. D. E. and Ybot-Gonzalez, P. (2011). Regional differences in the expression of laminin isoforms during mouse neural tube development. *Matrix Biol.* **30**, 301-309.

Danielian, P. S., Muccino, D., Rowitch, D. H., Michael, S. K. and McMahon, A. P. (1998). Modification of gene activity in mouse embryos in utero by a tamoxifen-inducible form of Cre recombinase. *Curr. Biol.* **8**, 1323-1326.

Dickinson, M. E., Selleck, M. A., McMahon, A. P. and Bronner-Fraser, M. (1995). Dorsalization of the neural tube by the non-neural ectoderm. *Development* **121**, 2099-2106.

Drake, J. M., Barnes, J. M., Madsen, J. M., Domann, F. E., Stipp, C. S. and Henry, M. D. (2010). ZEB1 coordinately regulates laminin-332 and 4 integrin expression altering the invasive phenotype of prostate cancer cells. *J. Biol. Chem.* **285**, 33940-33948.

Gao, X., Vockley, C. M., Pauli, F., Newberry, K. M., Xue, Y., Randell, S. H., Reddy, T. E. and Hogan, B. L. M. (2013). Evidence for multiple roles for grainyhead-like 2 in the establishment and maintenance of human mucociliary airway epithelium. *Proc. Natl. Acad. Sci. USA* **110**, 9356-9361.

Geelen, J. A. G. and Langman, J. (1979). Ultrastructural observations on closure of the neural tube in the mouse. *Anat. Embryol.* **156**, 73-88.

Gustavsson, P., Copp, A. J. and Greene, N. D. E. (2008). Grainyhead genes and mammalian neural tube closure. *Birth Defects Res. A Clin. Mol. Teratol.* **82**, 728-735.

Hackett, D. A., Smith, J. L. and Schoenwolf, G. C. (1997). Epidermal ectoderm is required for full elevation and for convergence during bending of the avian neural plate. *Dev. Dyn.* **210**, 397-406.

Harris, M. J. and Juriloff, D. M. (2010). An update to the list of mouse mutants with neural tube closure defects and advances toward a complete genetic perspective of neural tube closure. *Birth Defects Res. A Clin. Mol. Teratol.* **88**, 653-669.

Hildebrand, J. D. and Soriano, P. (1999). Shroom, a PDZ domain–containing actin-binding protein, is required for neural tube morphogenesis in mice. *Cell* **99**, 485-497.

Holmes, G. and Niswander, L. (2001). Expression of slit-2 and slit-3 during chick development. *Dev. Dyn.* **222**, 301-307.

Honarpour, N., Gilbert, S. L., Lahn, B. T., Wang, X. and Herz, J. (2001). Apaf-1 deficiency and neural tube closure defects are found in fog mice. *Proc. Natl. Acad. Sci. USA* **98**, 9683-9687.

Huangfu, D., Liu, A., Rakeman, A. S., Murcia, N. S., Niswander, L. and Anderson, K. V. (2003). Hedgehog signalling in the mouse requires intraflagellar transport proteins. *Nature* **426**, 83-87.

Ishibashi, M., Ang, S. L., Shiota, K., Nakanishi, S., Kageyama, R. and Guillemot, F. (1995). Targeted disruption of mammalian hairy and Enhancer of split homolog-1 (HES-1) leads to up-regulation of neural helix-loop-helix factors, premature neurogenesis, and severe neural tube defects. *Genes Dev.* **9**, 3136-3148.

Itasaki, N. (2003). Wise, a context-dependent activator and inhibitor of Wnt signalling. *Development* **130**, 4295-4305.

Jacobson, A. G. and Moury, J. D. (1995). Tissue boundaries and cell behavior during neurulation. *Dev. Biol.* **171**, 98-110.

Kassai, Y., Munne, P., Hotta, Y., Penttilä, E., Kavanagh, K., Ohbayashi, N., Takada, S., Thesleff, I., Jernvall, J. and Itoh, N. (2005). Regulation of mammalian tooth cusp patterning by ectodin. *Science* **309**, 2067-2070.

Kiso, H., Takahashi, K., Saito, K., Togo, Y., Tsukamoto, H., Huang, B., Sugai, M., Shimizu, A., Tabata, Y., Economides, A. N. et al. (2014). Interactions between BMP-7 and USAG-1 (uterine sensitization-associated gene-1) regulate supernumerary organ formations. *PLoS ONE* **9**, e96938.

Lardelli, M., Williams, R., Mitsiadis, T. and Lendahl, U. (1996). Expression of the Notch 3 intracellular domain in mouse central nervous system progenitor cells is lethal and leads to disturbed neural tube development. *Mech. Dev.* **59**, 177-190.

Larjava, H., Plow, E. F. and Wu, C. (2008). Kindlins: essential regulators of integrin signalling and cell–matrix adhesion. *EMBO Rep.* **9**, 1203-1208.

Laurikkala, J., Kassai, Y., Pakkasjärvi, L., Thesleff, I. and Itoh, N. (2003). Identification of a secreted BMP antagonist, ectodin, integrating BMP, FGF, and SHH signals from the tooth enamel knot. *Dev. Biol.* **264**, 91-105.

Leonard, J. R., Klocke, B. J., D'Sa, C., Flavell, R. A. and Roth, K. A. (2002). Strain-dependent neurodevelopmental abnormalities in caspase-3-deficient mice. *J. Neuropathol. Exp. Neurol.* **61**, 673-677.

Lim, J. and Thiery, J. P. (2012). Epithelial-mesenchymal transitions: insights from development. *Development* **139**, 3471-3486.

Liu, A., Joyner, A. L. and Turnbull, D. H. (1998). Alteration of limb and brain patterning in early mouse embryos by ultrasound-guided injection of Shh-expressing cells. *Mech. Dev.* **75**, 107-115.

Liu, J., Welm, B., Boucher, K. M., Ebbert, M. T. and Bernard, P. S. (2012). TRIM29 functions as a tumor suppressor in nontumorigenic breast cells and invasive ER+ breast cancer. *Am. J. Pathol.* **180**, 839-847.

Lucas, J. M., Heinlein, C., Kim, T., Hernandez, S. A., Malik, M. S., True, L. D., Morrissey, C., Corey, E., Montgomery, B., Mostaghel, E. et al. (2014). The androgen-regulated protease TMPRSS2 activates a proteolytic cascade involving components of the tumor microenvironment and promotes prostate cancer metastasis. *Cancer Discov.* **4**, 1310-1325.

Massarwa, R. and Niswander, L. (2013). In toto live imaging of mouse morphogenesis and new insights into neural tube closure. *Development* **140**, 226-236.

Micalizzi, D. S. and Ford, H. L. (2009). Epithelial–mesenchymal transition in development and cancer. *Future Oncol.* **5**, 1129-1143.

Mlacki, M., Kikulska, A., Krzywinska, E., Pawlak, M. and Wilanowski, T. (2015). Recent discoveries concerning the involvement of transcription factors from the Grainyhead-like family in cancer. *Exp. Biol. Med. (Maywood)* **240**, 1396-1401.

Morita, H., Kajiura-Kobayashi, H., Takagi, C., Yamamoto, T. S., Nonaka, S. and Ueno, N. (2012). Cell movements of the deep layer of non-neural ectoderm underlie complete neural tube closure in Xenopus. *Development* **139**, 1417-1426.

Morriss-Kay, G. and Tuckett, F. (1985). The role of microfilaments in cranial neurulation in rat embryos: effects of short-term exposure to cytochalasin D. *J. Embryol. Exp. Morphol.* **88**, 333-348.

Mostov, K. E., Mitaka, T., Miyajima, A. and Senga, N. T. (2012). Grainyhead-like 2 regulates epithelial morphogenesis by establishing functional tight junctions through the organization of a molecular network among claudin3, claudin4, and Rab25. *Mol. Biol. Cell* **23**, 2845-2855.

Moury, J. D. and Schoenwolf, G. C. (1995). Cooperative model of epithelial shaping and bending during avian neurulation: autonomous movements of the neural plate, autonomous movements of the epidermis, and interactions in the neural plate/epidermis transition zone. *Dev. Dyn.* **204**, 323-337.

Muzumdar, M. D., Tasic, B., Miyamichi, K., Li, L. and Luo, L. (2007). A global double-fluorescent Cre reporter mouse. *Genesis* **45**, 593-605.

Pulkkinen, L., Christiano, A. M., Airenne, T., Haakana, H., Tryggvason, K. and Uitto, J. (1994). Mutations in the gamma 2 chain gene (LAMC2) of kalinin/laminin 5 in the junctional forms of epidermolysis bullosa. *Nat. Genet.* **6**, 293-298.

Pyrgaki, C., Trainor, P., Hadjantonakis, A.-K. and Niswander, L. (2010). Dynamic imaging of mammalian neural tube closure. *Dev. Biol.* **344**, 941-947.

Pyrgaki, C., Liu, A. and Niswander, L. (2011). Grainyhead-like 2 regulates neural tube closure and adhesion molecule expression during neural fold fusion. *Dev. Biol.* **353**, 38-49.

Rhee, J. M., Pirity, M. K., Lackan, C. S., Long, J. Z., Kondoh, G., Takeda, J. and Hadjantonakis, A.-K. (2006). In vivo imaging and differential localization of lipid-modified GFP-variant fusions in embryonic stem cells and mice. *Genesis* **44**, 202-218.

Rifat, Y., Parekh, V., Wilanowski, T., Hislop, N. R., Auden, A., Ting, S. B., Cunningham, J. M. and Jane, S. M. (2010). Regional neural tube closure defined by the Grainy head-like transcription factors. *Dev. Biol.* **345**, 237-245.

Roberts, A., Goff, L., Pertea, G., Kim, D., Kelley, D. R., Pimentel, H., Salzberg, S. L., Rinn, J. L., Pachter, L. and Trapnell, C. (2012). Differential gene and transcript expression analysis of RNA-seq experiments with TopHat and Cufflinks. *Nat. Protoc.* **7**, 562-578.

Sausedo, R. A., Smith, J. L. and Schoenwolf, G. C. (1997). Role of nonrandomly oriented cell division in shaping and bending of the neural plate. *J. Comp. Neurol.* **381**, 473-488.

Selleck, M. A. and Bronner-Fraser, M. (1995). Origins of the avian neural crest: the role of neural plate-epidermal interactions. *Development* **121**, 525-538.

Siegel, D. H., Ashton, G. H. S., Penagos, H. G., Lee, J. V., Feiler, H. S., Wilhelmsen, K. C., South, A. P., Smith, F. J. D., Prescott, A. R., Wessagowit, V. et al. (2003). Loss of kindlin-1, a human homolog of the Caenorhabditis elegans actin–extracellular-matrix linker protein UNC-112, causes Kindler syndrome. *Am. J. Hum. Genet.* **73**, 174-187.

Sin, S., Bonin, F., Petit, V., Meseure, D., Lallemand, F., Bieche, I., Bellahcene, A., Castronovo, V., de Wever, O., Gespach C. et al. (2011). Role of the focal adhesion protein Kindlin-1 in breast cancer growth and lung metastasis. *J. Natl. Cancer Inst.* **103**, 1323-1337.

Steventon, B., Carmona-Fontaine, C. and Mayor, R. (2005). Genetic network during neural crest induction: from cell specification to cell survival. *Semin. Cell Dev. Biol.* **16**, 647-654.

Trapnell, C., Roberts, A., Goff, L., Pertea, G., Kim, D., Kelley, D. R., Pimentel, H., Salzberg, S. L., Rinn, J. L. and Pachter, L. (2012). Differential gene and transcript expression analysis of RNA-seq experiments with TopHat and Cufflinks. *Nat. Protoc.* **7**, 562-578.

Ussar, S., Moser, M., Widmaier, M., Rognoni, E., Harrer, C., Genzel-Boroviczeny, O. and Fässler, R. (2008). Loss of Kindlin-1 causes skin atrophy and lethal neonatal intestinal epithelial dysfunction. *PLoS Genet.* **4**, e1000289.

Walentin, K., Hinze, C., Werth, M., Haase, N., Varma, S., Morell, R., Aue, A., Pötschke, E., Warburton, D., Qiu, A. et al. (2015). A Grhl2-dependent gene

Development (2016) 143, 1192-1204 doi:10.1242/dev.129825

network controls trophoblast branching morphogenesis. *Development* **142**, 1125-1136.

Warzecha, C. C., Sato, T. K., Nabet, B., Hogenesch, J. B. and Carstens, R. P. (2009). ESRP1 and ESRP2 Are Epithelial Cell-Type-Specific Regulators of FGFR2 Splicing. *Mol. Cell* **33**, 591-601.

Warzecha, C. C., Jiang, P., Amirikian, K., Dittmar, K. A., Lu, H., Shen, S., Guo, W., Xing, Y. and Carstens, R. P. (2010). An ESRP-regulated splicing programme is abrogated during the epithelial–mesenchymal transition. *EMBO J.* **29**, 3286-3300.

Werth, M., Walentin, K., Aue, A., Schonheit, J., Wuebken, A., Pode-Shakked, N., Vilianovitch, L., Erdmann, B., Dekel, B., Bader, M. et al. (2010). The transcription factor grainyhead-like 2 regulates the molecular composition of the epithelial apical junctional complex. *Development* **137**, 3835-3845.

Wilde, J. J., Petersen, J. R. and Niswander, L. A. (2014). Genetic, epigenetic, and environmental contributions to neural tube closure. *Annu. Rev. Genet.* **48**, 583-611.

Xiang, J., Fu, X., Ran, W., Chen, X., Hang, Z., Mao, H. and Wang, Z. (2013). Expression and role of grainyhead-like 2 in gastric cancer. *Med. Oncol.* **30**, 714.

Xu, W., Baribault, H. and Adamson, E. D. (1998). Vinculin knockout results in heart and brain defects during embryonic development. *Development* **125**, 327-337.

Yamaguchi, Y. and Miura, M. (2013). How to form and close the brain: insight into the mechanism of cranial neural tube closure in mammals. *Cell. Mol. Life Sci.* **70**, 3171-3186.

Yamaguchi, Y., Shinotsuka, N., Nonomura, K., Takemoto, K., Kuida, K., Yosida, H. and Miura, M. (2011). Live imaging of apoptosis in a novel transgenic mouse highlights its role in neural tube closure. *J. Cell Biol.* **195**, 1047-1060.

Ybot-Gonzalez, P., Cogram, P., Gerrelli, D. and Copp, A. J. (2002). Sonic hedgehog and the molecular regulation of mouse neural tube closure. *Development* **129**, 2507-2517.

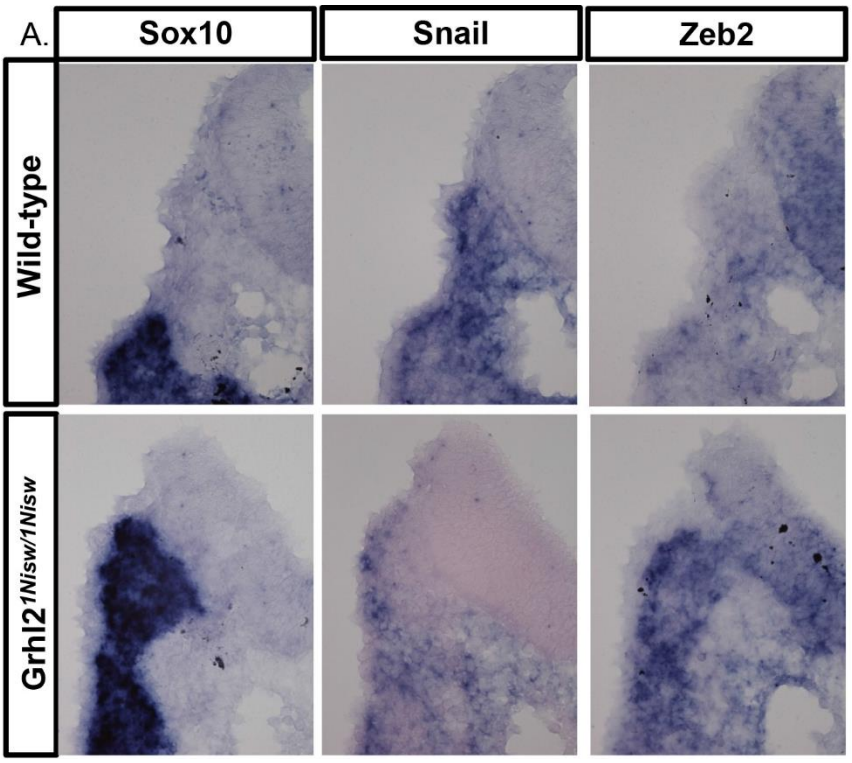

Fig. S1. *Sox10, Snail* and *Zeb2* expression patterns are similar in wild-type and *Grhl2* mutant embryos. RNA *in situ* hybridization was performed on transverse sections from E9.5 (17-20 somites) wild-type and *Grhl2*$^{1Nisw/1Nisw}$ embryos to visualize the expression patterns of *Sox10*, *Snail* and *Zeb2*. All genes are expressed in similar patterns in migrating neural crest cells in wild-type and *Grhl2* mutant embryos.

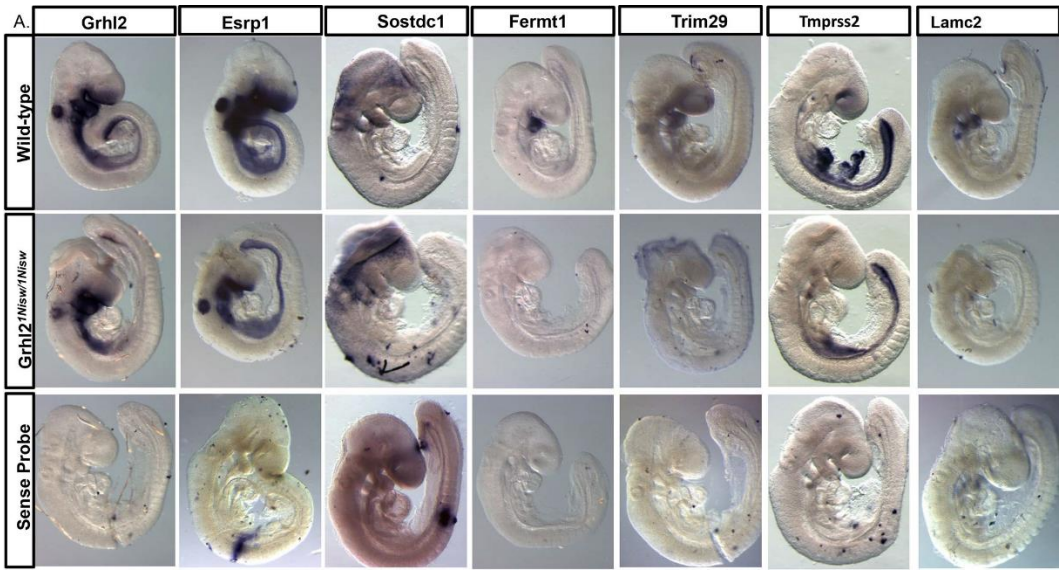

Fig. S2. *Esrp1*, *Sostdc1*, *Fermt1*, *Trim29*, *Tmprss2* and *Lamc2* expression patterns are altered in *Grhl2* mutant embryos. Whole mount *in situ* hybridization was performed on E9.5 (17-20 somites) wild-type and *Grhl2*$^{1Nisw/1Nisw}$ embryos to obtain mRNA expression patterns for *Esrp1*, *Sostdc1*, *Fermt1*, *Trim29*, *Tmprss2* and *Lamc2* in comparison to *Grhl2* expression. All genes except *Sostdc1* show altered expression patterns in *Grhl2* mutant embryos. No staining was visible with use of sense probes.

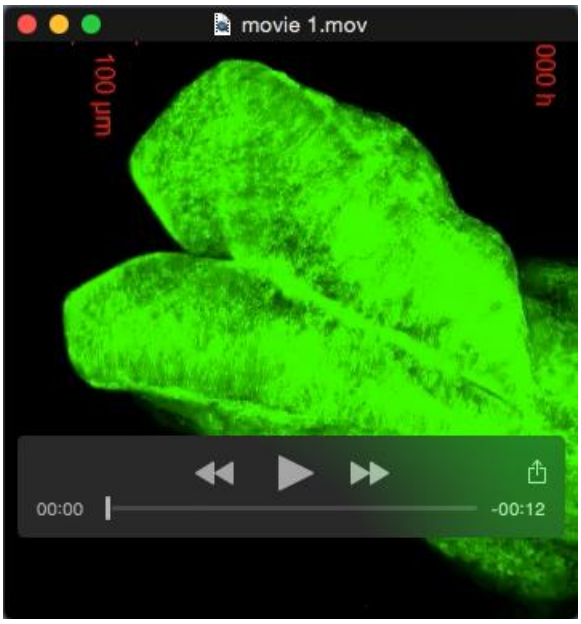

Movie 1. Live imaging of Myr-venus wild-type embryo undergoing neural tube closure. Time-lapse imaging of dorsal view of neural tube closure beginning at the 11 somite stage. Embryos express the Myr-venus transgene which constitutively highlights all cell membranes. 15 to 20 *z*-plane images were taken at 20 µm intervals continuously over an 8 hour period and combined in a maximum intensity projection. Over the course of imaging, the cranial neural folds bend toward the midline and neural tube closure proceeds by zippering rostral from closure point 1. Non-neural ectoderm is a smooth, intact epithelial layer with minimal membrane dynamics within the epithelial sheet. Scale bar = 100µm.

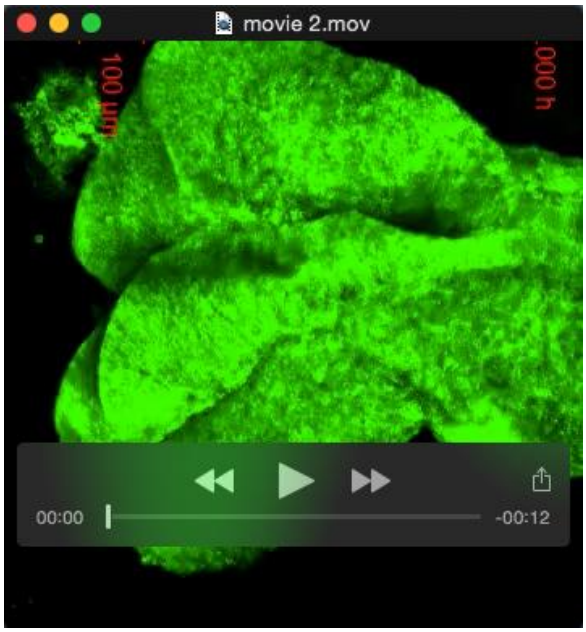

Movie 2. Live imaging of Myr-venus:*Grhl2*$^{1Nisw/1Nisw}$ embryo undergoing neural tube closure. Time-lapse imaging of dorsal view of neural tube closure beginning at the 11 somite stage. Embryos express the Myr-venus transgene which constitutively highlights all cell membranes. 15 to 20 *z*-plane images were taken at 20 µm intervals continuously over an 8 hour period and combined in a maximum intensity projection. Over the course of imaging, neural tube closure initially proceeds by zippering rostral from closure point 1; however, the neural folds fall away from each other impeding further closure of the cranial neural tube. Non-neural ectoderm at anterior-most neural folds appears rough and wavy and has increased dynamic movements compared to wild-type embryos. Scale bar = 100µm.

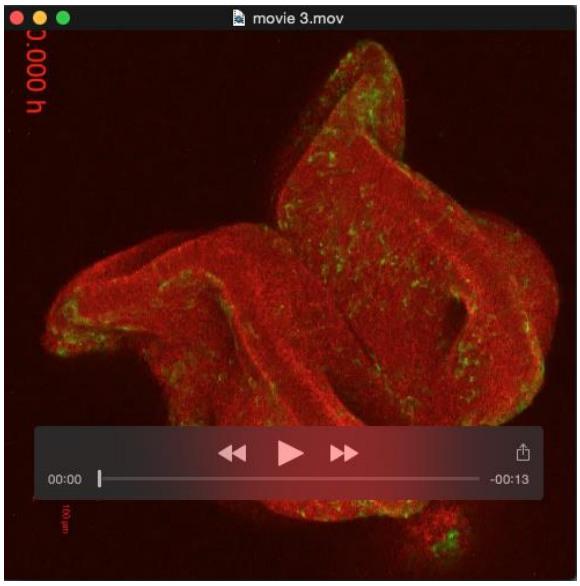

Movie 3. Live imaging of closure point 3 in a wild-type embryo. mTmG*:Grhl3-cre* embryos from a mTmG*:Grhl2*$^{1Nisw/+}$ X *Grhl3-cre:Grhl2*$^{1Nisw/+}$ genetic cross were mounted for imaging of closure point 3 starting at the 11 somite stage. Embryos express the mTmG transgene which constitutively highlights all cell membranes in red fluorescent protein (mTomato) and highlights the membranes of NNE cells expressing *Grhl3-cre* in green fluorescent protein (GFP). 15 to 20 *z*-plane images were taken at 20 μm intervals continuously over a 10 hour period and combined in a maximum intensity projection. Neural folds bend and move toward the midline where they meet and adhere to form closure point 3 within 6 hours of imaging. As the neural folds approach the midline, NNE cells are tightly associated with one another at the border between the NE and NNE as evidenced by the bright uninterrupted line of membrane GFP. Scale bar = 100μm.

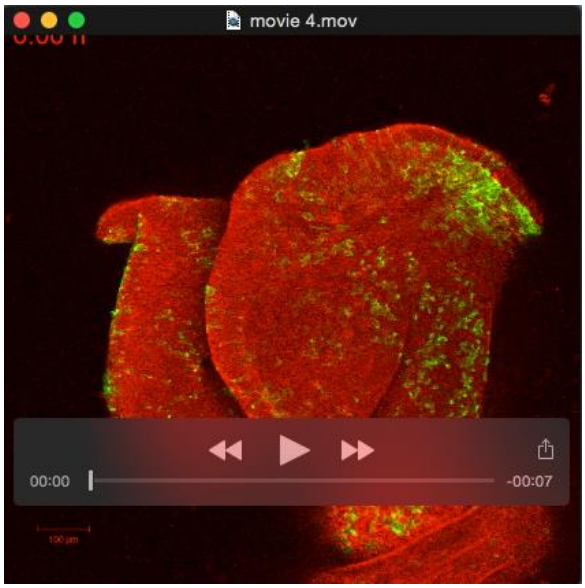

Movie 4. Live imaging of closure point 3 in a *Grhl2*$^{1Nisw/1Nisw}$ mutant embryo. Homozygous *Grhl2*$^{1Nisw/1Nisw}$ mutant embryos from a mTmG*:Grhl2*$^{1Nisw/+}$ X *Grhl3-cre:Grhl2*$^{1Nisw/+}$ genetic cross were mounted for imaging of closure point 3 starting at the 11 somite stage. Embryos express the mTmG transgene which constitutively highlights all cell membranes in red fluorescent protein (mTomato) and highlights the membranes of NNE cells expressing *Grhl3-cre* in green fluorescent protein (GFP). 15 to 20 *z*-plane images were taken at 20 μm intervals continuously over a 10 hour period and combined in a maximum intensity projection. Neural folds are unable to bend toward the midline and instead curl outward and fall away from each other. The tight association of NNE cells at the border with the NE is disrupted and some NNE cells exhibit highly dynamic movement. Scale bar = 100μm.

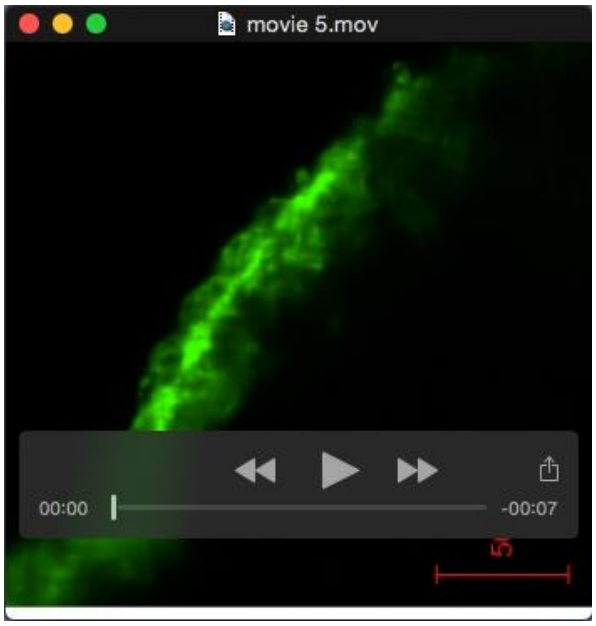

Movie 5. Live high-speed imaging of the non-neural ectoderm of a wild-type embryo. mTmG*:Grhl3-cre* embryos from a mTmG*:Grhl2*$^{1Nisw/+}$ X *Grhl3-cre:Grhl2*$^{1Nisw/+}$ genetic cross were mounted for imaging of the midbrain/hindbrain region starting at the 11 somite stage. Embryos express the mTmG transgene which constitutively highlights all cell membranes in red fluorescent protein (mTomato) and highlights the membranes of NNE cells expressing *Grhl3-cre* in green fluorescent protein (GFP). 15 *z*-plane images were taken at 3 μm intervals every 15 seconds for 15 minutes with a Zeiss 5Live confocal microscope system. Images were acquired using a Plan-Achromat 10X/0.45 objective at 2.0X zoom in and combined in a maximum intensity projection. Scale bar = 50μm.

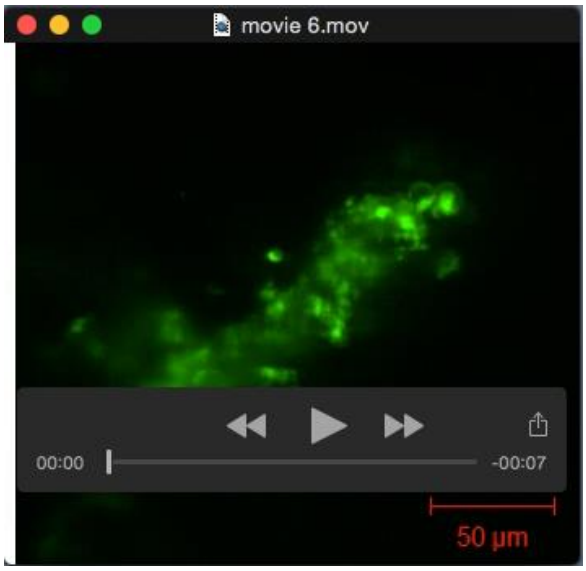

Movie 6. Live high-speed imaging of the non-neural ectoderm of a *Grhl2*$^{1Nisw/1Nisw}$ mutant embryo. Homozygous *Grhl2*$^{1Nisw/1Nisw}$ mutant embryos from a mTmG*:Grhl2*$^{1Nisw/+}$ X *Grhl3-cre:Grhl2*$^{1Nisw/+}$ genetic cross were mounted for imaging of the midbrain/hindbrain region starting at the 11 somite stage. Embryos express the mTmG transgene which constitutively highlights all cell membranes in red fluorescent protein (mTomato) and highlights the membranes of NNE cells expressing *Grhl3-cre* in green fluorescent protein (GFP). 15 *z*-plane images were taken at 3 µm intervals every 15 seconds for 15 minutes with a Zeiss 5Live confocal microscope system. Images were acquired using a Plan-Achromat 10X/0.45 objective at 2.0X zoom in and combined in a maximum intensity projection. Scale bar = 50µm.

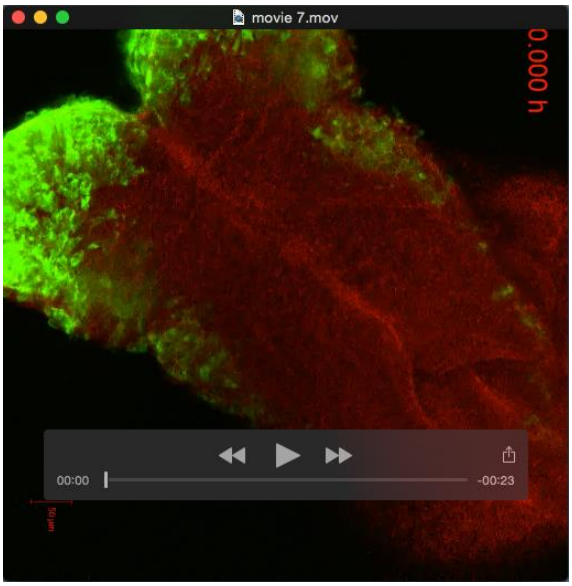

Movie 7. Live imaging of neural crest cell migration in a wild-type embryo. mTmG*:Wnt1-cre* embryos from a mTmG*:Grhl2*$^{1Nisw/+}$ X *Wnt1-cre:Grhl2*$^{1Nisw/+}$ genetic cross were mounted for imaging of a dorsal view of cranial neural tube closure starting at the 7 somite stage. Embryos express the mTmG transgene which constitutively highlights all cell membranes in red fluorescent protein (mTomato) and highlights the membranes of neural crest cells expressing *Wnt1-cre* in green fluorescent protein (GFP). 15 to 20 *z*-plane images were taken at 20 μm intervals continuously over a 16 hour period and combined in a maximum intensity projection. Neural crest cells are evident within the cranial neural folds prior to neural tube closure. Neural crest cells can be seen to migrate under the NNE and away from the midline caudal to the zippering fork in the region that has already undergone closure. Scale bar = 50μm.

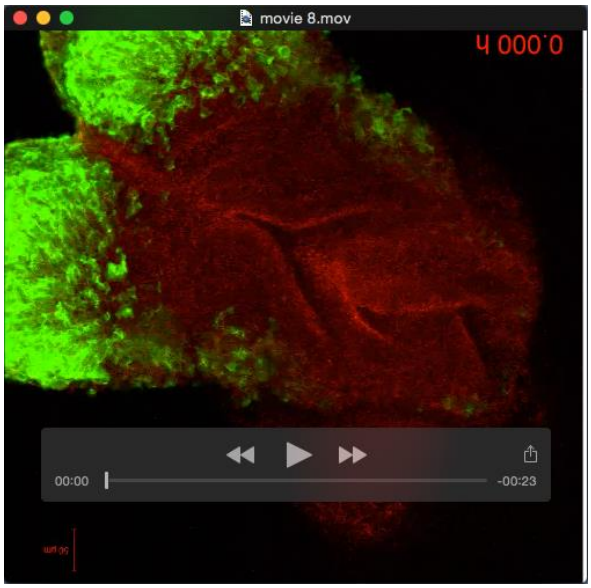

Movie 8. Live imaging of neural crest cell migration in a *Grhl2*$^{1Nisw/1Nisw}$ embryo. Homozygous *Grhl2*$^{1Nisw/1Nisw}$ mutant embryos from a mTmG*:Grhl2*$^{1Nisw/+}$ X *Wnt1-cre:Grhl2*$^{1Nisw/+}$ genetic cross were mounted for imaging of a dorsal view of cranial neural tube closure starting at the 7 somite stage. Embryos express the mTmG transgene which constitutively highlights all cell membranes in red fluorescent protein (mTomato) and highlights the membranes of neural crest cells expressing *Wnt1-cre* in green fluorescent protein (GFP). 15 to 20 *z*-plane images were taken at 20 μm intervals continuously over a 16 hour period and combined in a maximum intensity projection. Neural crest cells are evident within the cranial neural folds prior to neural tube closure. Neural crest cells can be seen to migrate under the NNE and away from the midline caudal to the zippering fork in the region that has already undergone closure. Scale bar = 50μm.

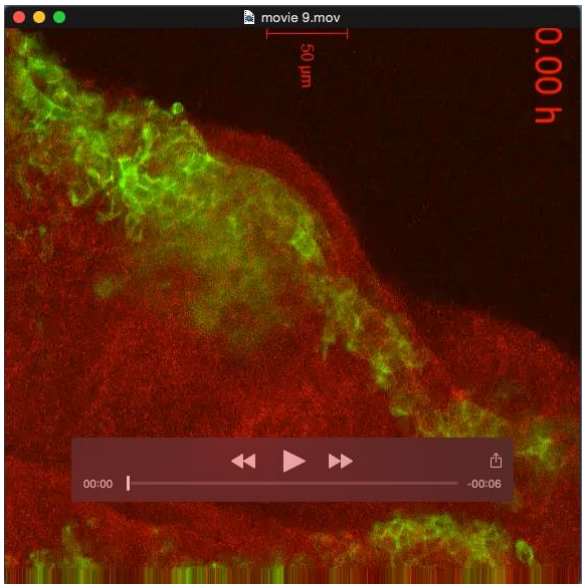

Movie 9. Live imaging of neural crest cells in the neural folds of a wild-type embryo. mTmG*:Wnt1-cre* embryos from a mTmG*:Grhl2*$^{1Nisw/+}$ X *Wnt1-cre:Grhl2*$^{1Nisw/+}$ genetic cross were mounted for imaging of a dorsal view of cranial neural tube closure starting at the 11 somite stage. Embryos express the mTmG transgene which constitutively highlights all cell membranes in red fluorescent protein (mTomato) and highlights the membranes of neural crest cells expressing *Wnt1-cre* in green fluorescent protein (GFP). 15 to 20 *z*-plane images were taken at 20 µm intervals continuously over a 6 hour period and combined in a maximum intensity projection. As the cranial neural fold just rostral to the zippering fork bends towards the midline, neural crest cells are evident within the fold prior to migration. The neural crest cell population appears to be restricted to the space below the non-neural ectoderm cell layer. Scale bar = 50µm.

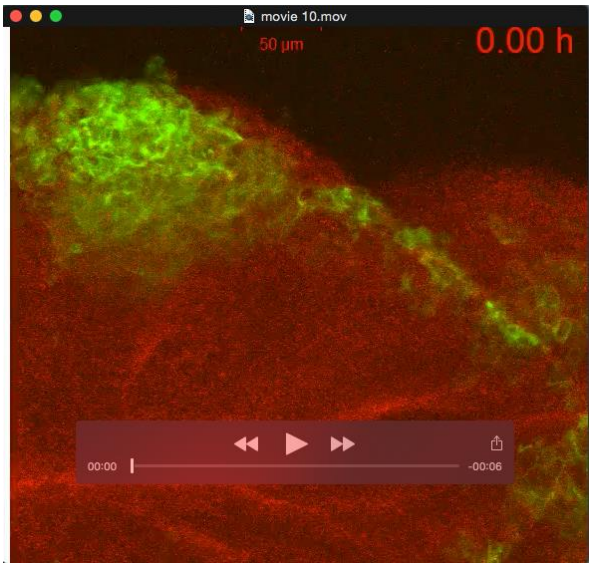

Movie 10. Live imaging of neural crest cells in the neural folds of a *Grhl2*$^{1Nisw/1Nisw}$ mutant embryo. Homozygous *Grhl2*$^{1Nisw/1Nisw}$ mutant embryos from a mTmG*:Grhl2*$^{1Nisw/+}$ X *Wnt1-cre:Grhl2*$^{1Nisw/+}$ genetic cross were mounted for imaging of a dorsal view of cranial neural tube closure starting at the 11 somite stage. Embryos express the mTmG transgene which constitutively highlights all cell membranes in red fluorescent protein (mTomato) and highlights the membranes of neural crest cells expressing *Wnt1-cre* in green fluorescent protein (GFP). 15 to 20 *z*-plane images were taken at 20 µm intervals continuously over a 6 hour period and combined in a maximum intensity projection. As the cranial neural fold just rostral to the zippering fork bends towards the midline, neural crest cells are evident within the fold prior to migration. While the majority of the neural crest cell population appears to reside within the space below the NNE, some NCCs are seen within the outer NNE cell layer and individual cell processes are evident external to the embryo. Scale bar = 50µm.

Table S1. Total number of embryos used in quantitation and live imaging experiments. All quantitation experiments were performed using multiple transverse tissue sections from stage-matched wild-type and *Grhl2* mutant embryos as indicated in the table. For all live imaging experiments, multiple embryos were mounted and imaged in each experiment as described in the methods. Post-imaging, embryos were collected and genotype was determined and recorded. Mutant phenotypes were determined based on careful comparison with both wild-type and *Grhl2*$^{1Nisw/+}$ heterozygous embryos for consistent differences.

Experiment	Genotype	Number of embryos	Sections per embryo
Histology Figure 1A-D, G	*Grhl2*$^{+/+}$	5	50
	Grhl2$^{1Nisw/1Nisw}$	7	50
ZO-1, Vimentin Figure 1E, F, H-J	*Grhl2*$^{+/+}$	4	10
	Grhl2$^{1Nisw/1Nisw}$	4	10
Live imaging movies 1 and 2	Myr-venus:*Grhl2*$^{+/+}$	7	
	Myr-venus:*Grhl2*$^{1Nisw/+}$	7	
	Myr-venus:*Grhl2*$^{1Nisw/1Nisw}$	3	
Live imaging movies 3 and 4	mTmG:*Grhl3-cre:Grhl2*$^{+/+}$	8	
	mTmG:*Grhl3-cre:Grhl2*$^{1Nisw/+}$	4	
	mTmG:*Grhl3-cre:Grhl2*$^{1Nisw/1Nisw}$	9	
Live imaging movies 5 and 6	mTmG:*Grhl3-cre:Grhl2*$^{+/+}$	1	
	mTmG:*Grhl3-cre:Grhl2*$^{1Nisw/+}$	4	
	mTmG:*Grhl3-cre:Grhl2*$^{1Nisw/1Nisw}$	4	
Live imaging movies 7-10	mTmG:*Wnt1-cre:Grhl2*$^{+/+}$	3	
	mTmG:*Wnt1-cre:Grhl2*$^{1Nisw/+}$	9	
	mTmG:*Wnt1-cre:Grhl2*$^{1Nisw/1Nisw}$	3	

Table S2. Antibodies and experimental conditions used in study.

For immunostaining of tissue cryosections, *Grhl2*$^{1Nisw/+}$ mice were mated and females checked for a vaginal plug (embryos at noon were considered to be 0.5 days post fertilization [E0.5]). Pregnant females were sacrificed and embryos dissected at E9-E9.5 and somites counted. Embryos were fixed in 4% PFA and processed for cryopreservation in OCT and sectioning at 12 μm. Rehydrated tissue was subjected to antigen retrieval with 0.01M sodium citrate if needed, followed by blocking in 0.1% Tween-20 in PBS with normal goat serum (NGS) for one hour at room temperature (RT) and incubation with primary antibody in blocking buffer overnight at 4°C. Secondary antibody incubation in 0.1% Tween-20 in PBS was performed for two hours RT, followed by Hoescht (in PBS) staining for 10 min at RT, and mounting with Faramount aqueous mounting media (Dako, cat#S3025). For immunostaining of cell lines, 5 x 10^4 cells were plated in 24-well plates on glass coverslips and incubated at 37^0C overnight. Cells were fixed with 4% PFA in PBS for 10 minutes at RT, followed by permeabilization (0.3% Triton-X in PBS (PBST)) for 10 minutes at RT, blocking (image-iT FX signal enhancer (Molecular Probes)) for 30 minutes at RT, and primary antibody incubation (PBST with NGS) overnight at 4°C. Secondary antibody incubation was performed in PBST for one hour at RT, Hoescht (1:1000 in PBS) for 10 minutes at RT, and mounted on glass slides with Faramount. All washes were performed with PBS. Fluorescent images were obtained on a LSM510 or LSM780 Meta confocal microscope (Zeiss). For quantitation of immunostainings, neural folds from 13-18 somite-matched embryos were analyzed using Imaris software. Batch parameters were used to identify ZO-1 punctate staining within the NNE followed by measurement determination between individual puncta. Surfaces were generated to form a volume of NNE in the x, y, and z planes in which total Vimentin fluorescence was identified and normalized as voxels per 1μm^3. For western blot analysis, all protein was collected by passive lysis in NP-40 lysis buffer with protease inhibitors (Protease inhibitor cocktail, Roche Diagnostics) for 30 min at 4°C on a rotating rack, followed by 20 minute centrifugation (13,000 RPM at 4˚C). Total protein in the supernatants was quantified by Bradford assay and the supernatants were stored at -80°C until needed. Laemmli sample buffer with β-mercaptoethanol (β-ME) was added to the protein supernatants (40μg total protein) and boiled for 5 min at 95°C, before running in 2-10% Bis-Tris gels (Invitrogen), except for Tmprss2 detection which required non-denaturing conditions. All blots were blocked for one hour at RT and incubated with primary antibodies overnight at 4°C. Blots were incubated with HRP-conjugated secondary antibodies one hour at RT and with ECL substrate (Perkin Elmer) for 5 minutes before imaging on a BioRad ChemiDoc MP imaging system. All washes were performed with TBST.

			Tissue Immunohistochemistry			Cell Line Immunohistochemistry		Western Blot		
Antibody	Company	Catalog #	Dilution	Antigen retreival	Goat serum %	Dilution	Goat serum %	Dilution	Block buffer 5% Milk	Ab dilution buffer
Rb anti-hu ZO-1	Invitrogen	40-2200	1:200	Yes	1%	1:250	1%			
Ms anti-Vimentin	Abcam	ab20346	1:150	Yes	1%	1:500	1%			
Rb anti-GFP	Life Technologies	G10362	1:100	No	5%					
Rb anti-hu Fibronectin	Sigma	F3648	1:300	No	5%					
Ms anti-hu E-cadherin	BD Biosciences	610181				1:500	1%			
Ms anti-N-cadherin	Invitrogen	33-3900				1:500	1%			
Ms anti-hu Grhl2	Abnova	H00079977-A01						1:500	TBST	5% Milk
Ms anti-Esrp1	Abnova	PAB16900						1:500	TBST	5% Milk
Rb anti-hu Sostdc1	Abgent	AP17397b						1:100	TBS	5% Milk
Rb anti-hu Kindlin	Abcam	ab68041						1:1000	TBST	5% Milk
Ms anti-hu Laminin γ-2	Santa Cruz Biotech	28330						1:250	TBST	5% Milk
Rb anti-hu Tmprss2	Abgent	AJ1774a						1:1000	TBS	TBST
Rb anti-ms GAPDH	Sigma	G9545						1:3000	TBST	5% Milk
Ms anti-rat β-tubulin	BD Biosciences	556321						1:3000	TBST	5% Milk
Gt anti-ms-HRP	Bio Rad Laboratorie	170-5047						1:3000		5% Milk
Gt anti-rb-HRP	Bio Rad Laboratorie	170-5046						1:3000		5% Milk
Gt anti-ms IgG2a-AF48	Life Technologies	A21131				1:1000				
Gt anti-ms IgG1-AF555	Life Technologies	A21127				1:1000				
Gt anti-rb IgG-AF555	Life Technologies	A21429	1:1000							
Gt anti-rb IgG-AF488	Life Technologies	A11008	1:1000			1:1000				
Gt anti-ms IgM-AF568	Life Technologies	A21043	1:1000			1:1000				
Hoescht			1:3000			1:3000				

Table S3. Histology and *In situ* hybridization conditions and probes used in this study. All *in situ* hybridization probes were generated using cDNA made from embryonic mouse total RNA with the primer pairs listed in this table. *Grhl2*$^{1Nisw/+}$ mice were mated and females checked for a vaginal plug (embryos at noon were considered to be 0.5 days post fertilization [E0.5]). Pregnant females were sacrificed and embryos dissected at E9-E9.5 and somites counted. Embryos were fixed in 4% PFA and processed for paraffin embedding and sectioning at 5 µm followed by staining with hematoxylin and eosin by standard methods or for cryopreservation in OCT and sectioning at 10 µm for *in situ* hybridization. Whole mount and section *in situ* hybridization was performed as described (Holmes et al., 2001; Liu et al., 1998) with digestion in 5µg/ml Proteinase K for 2 minutes (sections) or 6 minutes (whole mounts) using the probes detailed above. Bright-field images were obtained on a Nikon i80 compound microscope.

	Dilution			
Gene probed	whole mount	section	primers used	cloning backbone
Sox10		1:500	Kindly gifted by Dr. David Rowitch (UC San Francisco)	
Snail		1:250	Kindly gifted by Dr. Angela Nieto (Instituto de Neurociencias (CSIC-UMH))	
Zeb2		1:100	5′-TCCCACAGTAGCTCGTACACTCC-3' 5′-TAGTCTTGTGCTCCATCCAGCAAG-3′	Zero-blunt TOPO vector (Life Technologies)
Grhl2	1:100	1:500	Generated previously (Pyrgaki, C, 2011)	
Esrp1	1:100	1:500	Kindly gifted by Dr. Trevor Williams (UC Denver AMC)	
Sostdc1	1:100	1:500	5′-CTTCTTCCTGCCATTCATCTC-3' 5′-GGGTAGCAGATGCTTTCTAGTC-3′	Zero-blunt TOPO vector
Fermt1	1:100	1:500	5′-GACACCAGCCTTATCCACTATG-3′ 5′-TTCCAGGGTCACTTCCAAAC-3′	Zero-blunt TOPO vector
Trim29	1:100	1:500	5′-CCAAGGCAGAGAAGGAGACCGA-3′ 5′-CAACATGACGCATGCACACA-3′	Zero-blunt TOPO vector
Tmprss2	1:100	1:500	5′-CACTGTGTGGAAGAACCCCT-3′ 5′GTGGATTAGCTGTTCGCCCT-3′	Zero-blunt TOPO vector
Lamc2	1:50	1:250	5′-AAGGCTGATTCTCTCTCAAACC-3′ 5′-TCCAAGTTCAGACTCCCTATCT-3′	Zero-blunt TOPO vector